

Basic macros		Compatibility with language.def
Hooks	Defining babelensure	Macros for setting language files up
Shorhands		
	Language attributes	Macros for saving definitions
tags	Hyphens	Short
related to glyphs	Multiencoding strings	Macros
engine specific macros		Bidi layout
Redefinitions for bidi layout	Bidi footnotes	Creating languages and
reading ini files		Hyphen
rules for 'canadian' set to "l@english		
("language0). ReportedHyphen rules for 'australian' set to "l@ukenglish		
("language21). ReportedHyphen rules for 'newzealand' set to "l@ukenglish		
("language21). Reported		
english		



Politechnika Warszawska

W Y D Z I A Ł F I Z Y K I



# Praca dyplomowa inżynierska

na kierunku fizyka techniczna  
w specjalności fizyka komputerowa

Implementation of machine learning algorithms for particle  
identification in the CBM experiment

Julian Nowak

Numer albumu: 298198

promotor:  
dr hab. inż. Hanna Zbroszczyk, prof. nzw.

WARSZAWA 2022



## **Streszczenie**

---

Tytuł pracy: Tytuł

Streszczenie

Imię i nazwisko

*słowa kluczowe:*

*szablon, LaTeX, praca dyplomowa*

(podpis opiekuna naukowego)

(podpis dyplomanta)



## **Abstract**

---

Title of the thesis: Title

Abstract

*Keywords:*

*template, LaTeX, thesis*



## Oświadczenie o samodzielności wykonania pracy

---



Politechnika Warszawska

imię i nazwisko

nr indeksu

kierunek studiów

### Oświadczenie

Świadomy/-a odpowiedzialności karnej za składanie fałszywych zeznań oświadczam, że niniejsza praca dyplomowa została napisana przeze mnie samodzielnie, pod opieką kierującego pracą dyplomową.

Jednocześnie oświadczam, że:

- niniejsza praca dyplomowa nie narusza praw autorskich w rozumieniu ustawy z dnia 4 lutego 1994 roku o prawie autorskim i prawach pokrewnych (Dz.U. z 2006 r. Nr 90, poz. 631 z późn. zm.) oraz dóbr osobistych chronionych prawem cywilnym,
- niniejsza praca dyplomowa nie zawiera danych i informacji, które uzyskałem/-am w sposób niedozwolony,
- niniejsza praca dyplomowa nie była wcześniej podstawą żadnej innej urzędowej procedury związanej z nadawaniem dyplomów lub tytułów zawodowych,
- wszystkie informacje umieszczone w niniejszej pracy, uzyskane ze źródeł pisanych i elektronicznych, zostały udokumentowane w wykazie literatury odpowiednimi odnośnikami,
- znam regulacje prawne Politechniki Warszawskiej w sprawie zarządzania prawami autorskimi i prawami pokrewnymi, prawami własności przemysłowej oraz zasadami komercjalizacji.

Warszawa, dnia (data)

(czytelny podpis dyplomanta)



## Oświadczenie o udzieleniu Uczelni licencji do pracy

---



Politechnika Warszawska

imię i nazwisko

nr indeksu

kierunek studiów

### Oświadczenie studenta w przedmiocie udzielenia licencji Politechnice Warszawskiej

Oświadczam, że jako autor / współautor\* pracy dyplomowej pt.

*Tytuł pracy*

udzielam / nie udzielam\* Politechnice Warszawskiej nieodpłatnej licencji na niewyłączne, nieograniczone w czasie, umieszczenie pracy dyplomowej w elektronicznych bazach danych oraz udostępnianie pracy dyplomowej w zamkniętym systemie bibliotecznym Politechniki Warszawskiej osobom zainteresowanym. Licencja na udostępnienie pracy dyplomowej nie obejmuje wyrażenia zgody na wykorzystywanie pracy dyplomowej na żadnym innym polu eksploatacji, w szczególności kopiowania pracy dyplomowej w całości lub w części, utrwalania w innej formie czy zwielokrotniania.

Warszawa, dnia (data)

(czytelny podpis dyplomanta)

\* - niepotrzebne skreślić



# Contents

<b>1</b>	<b>Introduction</b>	<b>13</b>
<b>2</b>	<b>Physical motivation</b>	<b>15</b>
2.1	Standard Model . . . . .	15
2.2	Quantum chromodynamics . . . . .	16
2.3	Heavy-ion collisions . . . . .	18
2.4	Reconstruction of short-lived strange particles . . . . .	18
<b>3</b>	<b>FAIR and CBM</b>	<b>21</b>
3.1	FAIR . . . . .	21
3.2	CBM experiment . . . . .	21
3.2.1	CBM setup . . . . .	22
3.2.2	Monte Carlo models . . . . .	22
<b>4</b>	<b>Machine learning</b>	<b>25</b>
4.1	XGBoost . . . . .	26
<b>5</b>	<b>Traditional methods of particles identification</b>	<b>29</b>
5.1	Particle identification using the time-of-flight method . . . . .	29
5.2	Short-lived particles reconstruction . . . . .	30
5.2.1	PFSimple . . . . .	31
<b>6</b>	<b>Optimizing <math>K_s^0</math> reconstruction using ML</b>	<b>33</b>
6.1	Model preparation . . . . .	33
6.1.1	Data enriching . . . . .	34
6.1.2	Data cleaning . . . . .	34
6.1.3	Variables selection . . . . .	36
6.2	Model training . . . . .	38
6.2.1	Results for $p_{\text{beam}} = 12\text{A GeV}/c$ . . . . .	38
6.2.2	Results for $p_{\text{beam}} = 3.3\text{A GeV}/c$ . . . . .	44
6.2.3	Influence of the magnetic field scaling . . . . .	44
<b>7</b>	<b>"TOF" particles identification using ML</b>	<b>47</b>
7.1	Model preparation . . . . .	48
7.1.1	Data enriching . . . . .	48

7.1.2	Data cleaning . . . . .	48
7.1.3	Variables selection . . . . .	51
7.2	Model training . . . . .	51
7.2.1	Probability plots . . . . .	52
7.2.2	Confusion matrix . . . . .	54
7.2.3	Mass-squared distributions . . . . .	56
7.3	Analysis of the results . . . . .	57
<b>8</b>	<b>Discussion and summary</b>	<b>63</b>
<b>9</b>	<b>Appendix A</b>	<b>65</b>
<b>10</b>	<b>Appendix B</b>	<b>67</b>
<b>11</b>	<b>Appendix C</b>	<b>69</b>

# **Introduction**

Introduction introduction introduction introduction



# Physical motivation

## 2.1 Standard Model

The Standard Model, which was formulated in the '70s of the XXth century, describes the elementary particles and the interactions between them. It combines the theory of the elementary particles, quantum mechanics, quantum chromodynamics (strong interactions), and electroweak forces (unified description of the weak and electromagnetic forces). While most of its assumptions were confirmed in the '80s, the most recent one - the confirmation of the existence of the *Higgs boson*, dates from 2013. [1]

However, the Standard Model is not complete, it does not describe e.g., the gravitational forces, or the new findings such as the existence of the dark matter and the muon's magnetism [2]. While the explanation of these phenomena could prove the theory wrong, it describes well the majority of interactions between the matter.

According to the Standard model, there are two main classes of elementary particles: **fermions**, which constitute the matter, and **bosons**, which carry the interactions.

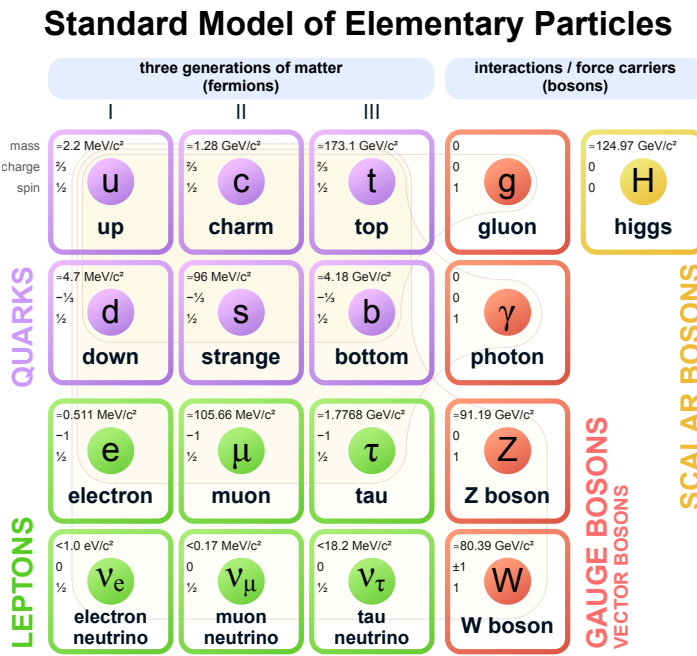


Figure 2.1: Standard Model of Elementary Particles [3]

Fermions follow the Fermi-Dirac statistics (hence the name), they have half odder integer spin and thus follow the **Pauli exclusion principle**. They can be divided into two groups: **leptons** and **quarks**. Leptons, unlike the quarks, have an integer charge number; they do not have the **color charge**, so they do not engage in strong interactions. There are three generations of the fermions:

I. quarks: *up* (*u*) and *down* (*d*); leptons: *electron* ( $e^-$ ) and *electron neutrino* ( $\nu_e$ )

II. quarks: *charm* (*c*) and *strange* (*s*) ; leptons: *muon* ( $\mu^-$ ) and *muon neutrino* ( $\nu_\mu$ )

III. quarks: *top* (*t*) and *bottom* (*b*); leptons: *tau* ( $\tau^-$ ) and *tau neutrino* ( $\nu_\tau$ )

Bosons follow (*nomen omen*) Bose-Einstein statistics, they have an integer spin. There are five elementary bosons carrying:

- strong forces: *gluons* (*g*)
- weak forces: bosons  $W^\pm$  and  $Z^0$
- electromagnetic forces: *photons* ( $\gamma$ )
- mass: *Higgs boson* (*H*)

## 2.2 Quantum chromodynamics

Quantum chromodynamics, a part of the Standard Model theory, describes the strong interactions between the quarks and gluons. It explains i.a. why quarks are confined in the hadrons[1]. According to this theory:

- there are three color charges: *Red*, *Green*, and *Blue* which are exchanged between the quarks via bosons - *gluons*
- gluons interact with both quarks and other gluons
- the strong interaction has a pulling character, the *color potential* can be described by this formula:

$$V(r) = -\frac{4}{3} \frac{\alpha_s}{r} + kr \quad (2.1)$$

where  $\alpha_s$  and  $k$  - coupling constants,  $r$  - distance. According to the formula 2.1, the magnitude of the force grows with distance, unless the latter is bigger than a certain threshold (as shown on Figure 2.2) - then, a new particle-antiparticle couple is created. This effect, called **quark confinement**, explains why the quarks cannot be separated and form **hadronic matter**. However, if the distance  $r$  is very small, and the energy of the system is big enough, there exists another state of matter called **quark-gluon plasma (QGP)** for which the quarks reach asymptotic freedom (asymptotic, as the strong interactions still do not allow the existence of free quarks).

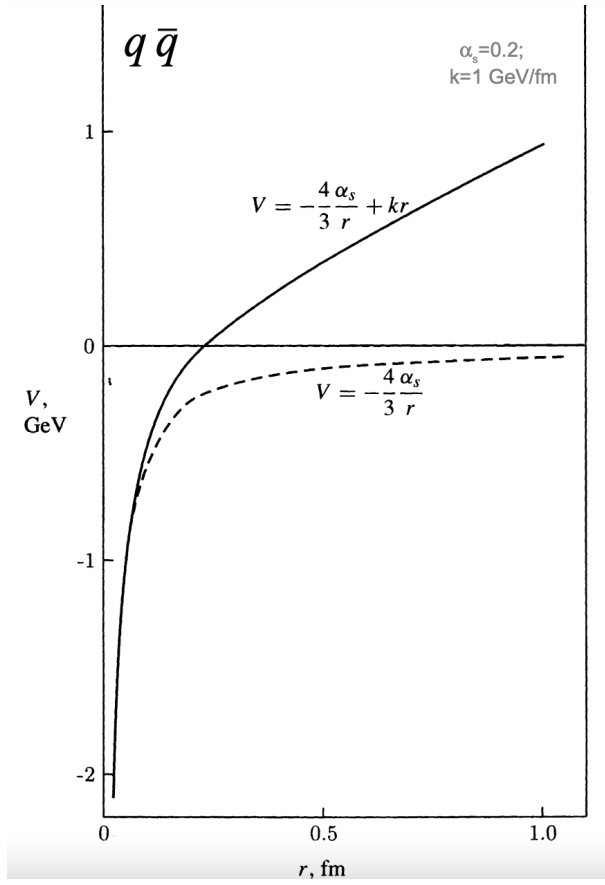
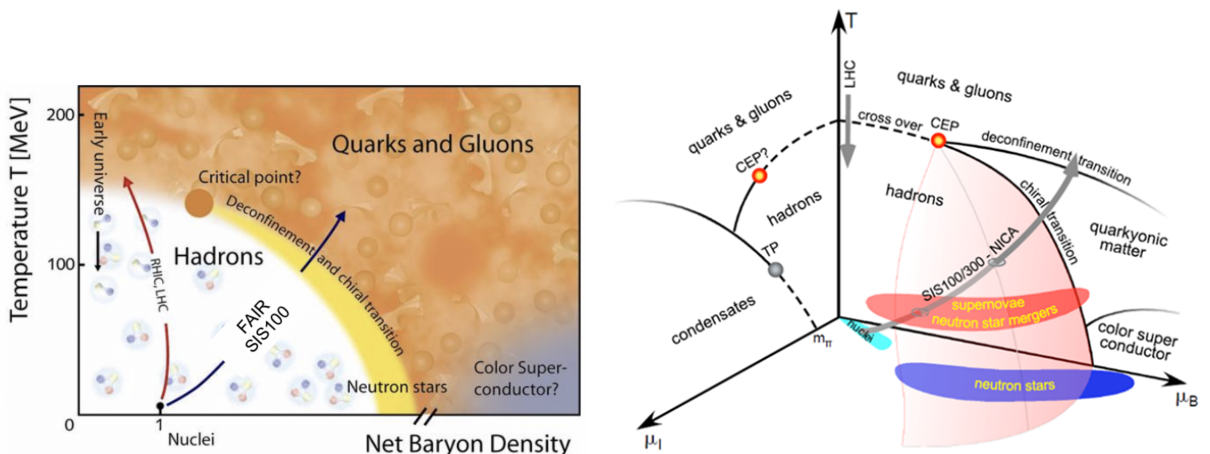


Figure 2.2: Dependence of the color charge potential and the distance between the quarks and gluons. At long distances, the binding energy is too high and a new particle-antiparticle pair is created [4]

As the matter can exist in both states: *hadronic matter* and *QGP*, the phase transition between the two is certain. The phase diagram can be presented on a 2D graph (with net baryon density on the x-axis and temperature on the y-axis) (Figure 2.3a), or a 3D graph (with isospin-chemical potential on the z-axis) (Figure 2.3b). The QCD matter diagram, especially the phase transition, is investigated by multiple high-energy physics experiments.



(a) 2D: net baryon density on the x-axis and temperature on the y-axis [5] (b) 3D: additional variable - isospin-chemical potential on the z-axis [6]

Figure 2.3: Phase diagram of the QCD matter

## 2.3 Heavy-ion collisions

Heavy-ion collisions at relativistic energies allow achieving both high temperature and high net baryon density, consequently creating *QGP* for a short time. In the *fixed-target* experiments, a heavy-ion is aimed at e.g., a foil; in the *collider* experiments, two heavy-ions are accelerated and then collided, allowing to achieve higher energies.

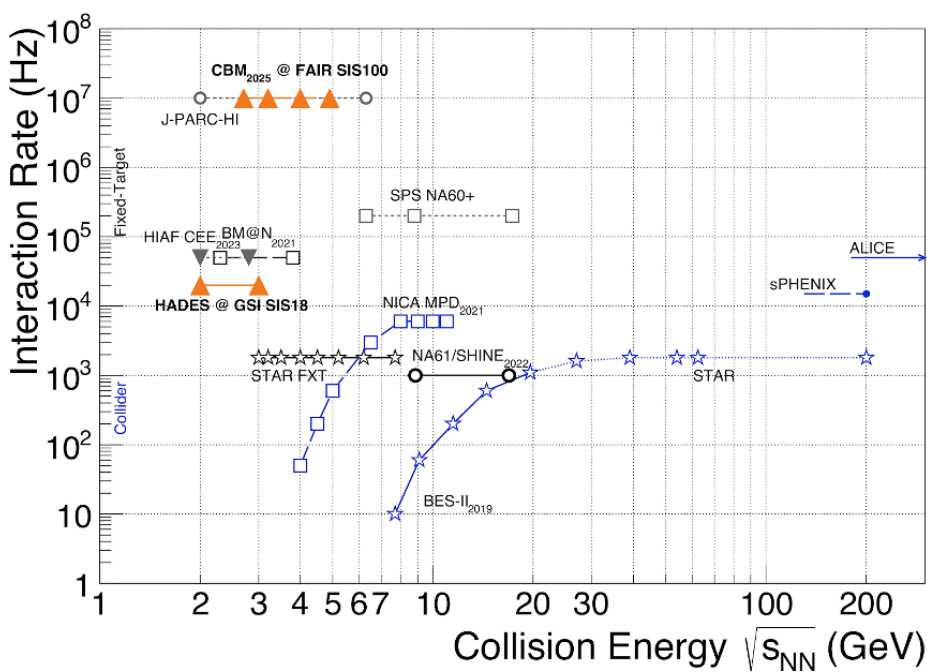


Figure 2.4: The "map" of the heavy-ion collision experiments [7]

Besides the type of setup, the high energy physics experiments also differ from one to another by i.e. achieved temperature, interaction rate, atomic number of the *bullet* (collided) ion, etc. The most important, current experiments are shown on the Figure 2.4. As we see also on both Figure 2.3a, and Figure 2.4, while the experiments at the Large Hadron Collider (LHC) in CERN aim for bigger collision energies and hence temperatures[8], the experiments performed (or planned) on SIS accelerators in FAIR aim for bigger interaction rates and consequently bigger net baryon density[9].

## 2.4 Reconstruction of short-lived strange particles

In the heavy-ion experiments, the strange quarks are only produced during collisions. Thus, they provide information about the evolution of nuclear matter. It is expected[10] that in the **mixed-phase** (when both nucleon and quark degrees of freedom are present), which can be produced at FAIR energies, the yield of strange particles could be comparable with particles composed of *u* and *d* quarks. To verify this, the reconstruction of strange particles, also short-lived ones like  $\Lambda^0$ ,  $\Xi^-$ ,  $K_S^0$  which cannot be detected directly, is important.

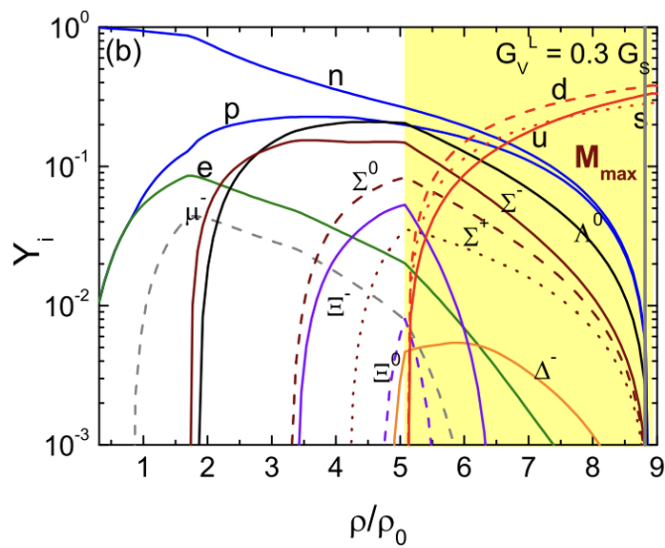


Figure 2.5: Particle population vs density (mixed-phase highlighted in yellow) [10]



# FAIR and CBM

## 3.1 FAIR

FAIR (*Facility for Antiproton and Ion Research*) is an international accelerator facility for the research with antiprotons and ions which is being developed and built in cooperation with international partners, i.a. Poland. FAIR is being built at the GSI Helmholtzzentrum für Schwerionenforschung in Darmstadt, Germany. The existing GSI accelerators will become part of the future FAIR facility and serve as the first acceleration stage[11]. The new accelerator, SIS 100, is foreseen to become operational in 2025[5]. The map of the existing facilities of GSI, and FAIR (which is still under construction) is shown on Figure 3.3. Several experiments will be held at FAIR: APPA, HADES, NUSTAR, PANDA, and CBM.

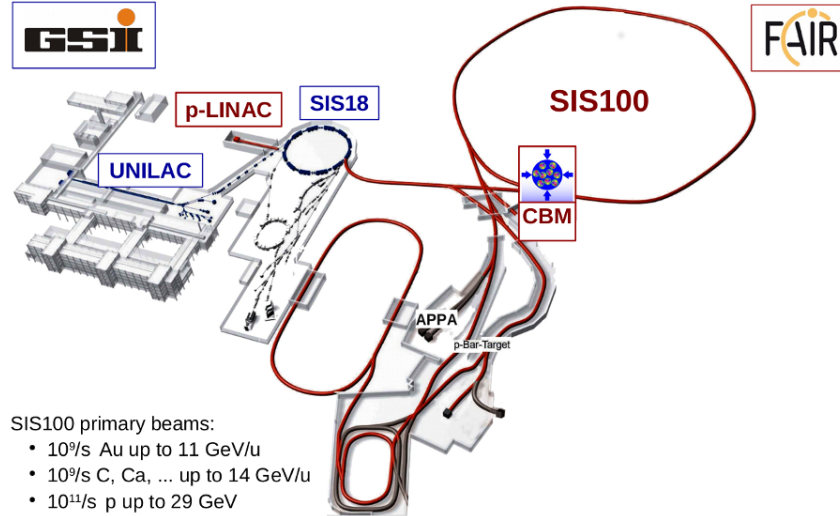


Figure 3.1: Map of FAIR[11]

## 3.2 CBM experiment

The CBM experiment will be held at the Facility for Antiproton and Ion Research. Its goal is the exploration of the QCD phase diagram in the region of high net baryon densities and moderate temperatures. It will allow i.a. studying the equation-of-state of nuclear matter at neutron star core densities. The measurements will be performed at reaction rates up to 10 MHz. It requires a highly efficient particle identification and reconstruction framework.[12]

### 3.2.1 CBM setup

In order to identify the particles coming from the collisions, the setup of 8 detectors is under development in FAIR (Figure 5.3).

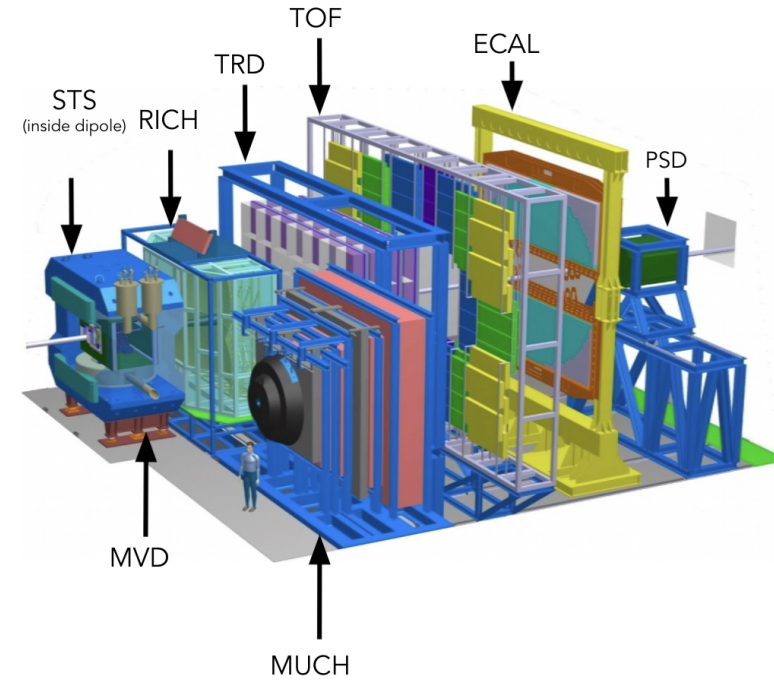


Figure 3.2: CBM setup[5]

The CBM detectors setup will consist of[5]:

- STS - Silicon Tracking System
- MVD - Micro Vertex Detector
- RICH - Ring Imaging Cherenkov Detector, replaceable with:
- MUCH - Muon Chamber System
- TRD - Transition Radiation Detector
- TOF - Time of Flight Detector
- ECAL - Electromagnetic Calorimeter
- PSD - Projectile Spectator Detector.

### 3.2.2 Monte Carlo models

As the main CBM accelerator, the SIS100, will not start functioning earlier than in 2025, the Monte Carlo models are handy in simulating the possible results and planning the actual setup of the experiment[5].

The majority of the simulations performed by the CBM Collaboration are performed using two Monte Carlo-based simulation packages: **URQMD** (Ultra relativistic Quantum Molecular Dynamics)[13], and **DCM-QGSM-SMM** (Dubna Cascade Model and Statistical Multifragmentation Model)[14]. Both models treat the production of new particles via the

formation and fragmentation of specific colored objects, strings. The differences between the models arise on different stages of a string formation and fragmentation.[14]

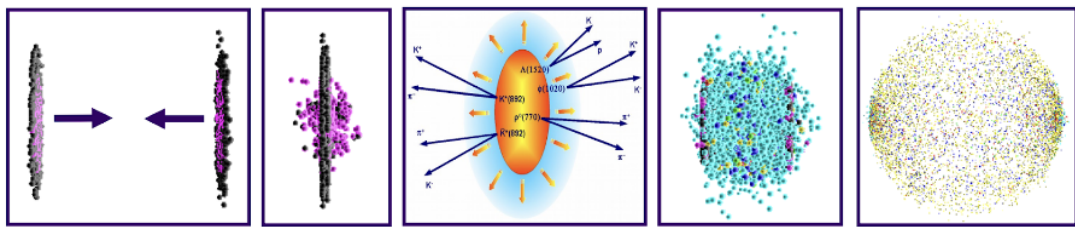


Figure 3.3: Visualisation of heavy-ion collisions in the URQMD model[15]

The data from the Monte Carlo models is later passed through **GEANT4** - a toolkit for simulating the passage of particles through matter.[16] The CBM setup is simulated in it, allowing to recreate the behaviour and work of different detectors and the influence of the construction elements. Finally, the simulated MDV, STS, RICH, TDR, TOF, and PSD hits are reconstructed into tracks and clusters and processed into a special data format, called *Analysis Tree*[17].



# Machine learning

The machine learning (ML) is a branch of **artificial intelligence (AI)** and computer science which focuses on the use of data and algorithms to imitate the way that humans learn, gradually improving its accuracy. Through the use of statistical methods, algorithms are trained to make classifications or predictions[18]. This term was first introduced in a paper from 1959, where the computer was trained to play the game of checkers[19]. The machine learning can be divided into three primary categories[18]:

- **supervised learning** - using labeled datasets to train algorithms that classify data or predict outcomes accurately. As input data is fed into the model, it adjusts its weights until the model has been fitted appropriately
- **unsupervised learning** - using machine learning algorithms to analyze and cluster unlabeled datasets. These algorithms discover hidden patterns or data groupings without the need for human intervention
- **reinforcement machine learning** - behavioral machine learning model that is similar to supervised learning, but the algorithm is not trained using sample data. This model learns using the trial and error method

The most known uses of ML are i.e. speech recognition, computer vision, recommendation engines. Furthermore, it has been also successfully used already in the high-energy physics (more specifically the subcategory of ML, the *deep learning*, which automates much of the feature extraction piece of the process, requiring less human intervention to learn), for tasks as simulating the calorimeter response in the LHCb experiment [20], and inspection of the silicon micro-strips of the STS detector in the CBM experiment[21].

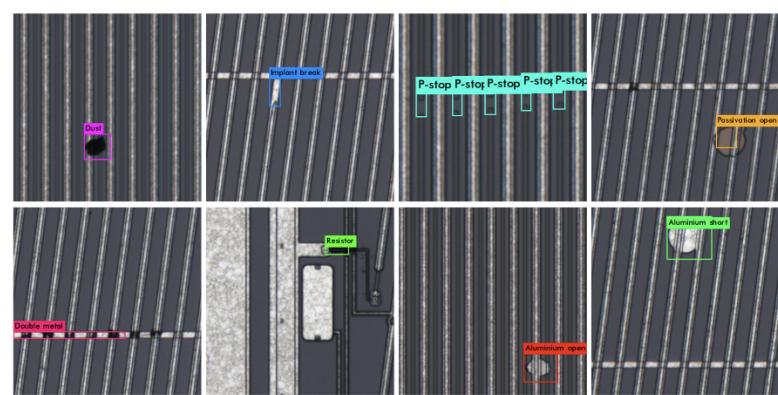


Figure 4.1: Various surface defects on the silicon sensor identified using deep neural network[21]

## 4.1 XGBoost

XGBoost is a **decision-tree-based, supervised** Machine Learning algorithm that uses gradient boosting, available as an open-source package [22]. It is highly efficient when used with e.g., tabular data.[23] It combines three elements:

- **Decision trees** - graphical representation of possible decisions based on certain conditions
- **Random Forest** - Selecting a random subset of features from multiple decision trees and *bagging* - making a decision based on the majority of their predictions
- **Gradient Boosting** - applying gradient descent algorithm to minimize the errors from random forests to train the algorithm[24]

Contrary to normal decision trees, it returns the **probability** of a certain decision (not a 0-1 decision) and trains itself given the error of its predictions (using mentioned before *gradient boosting*).

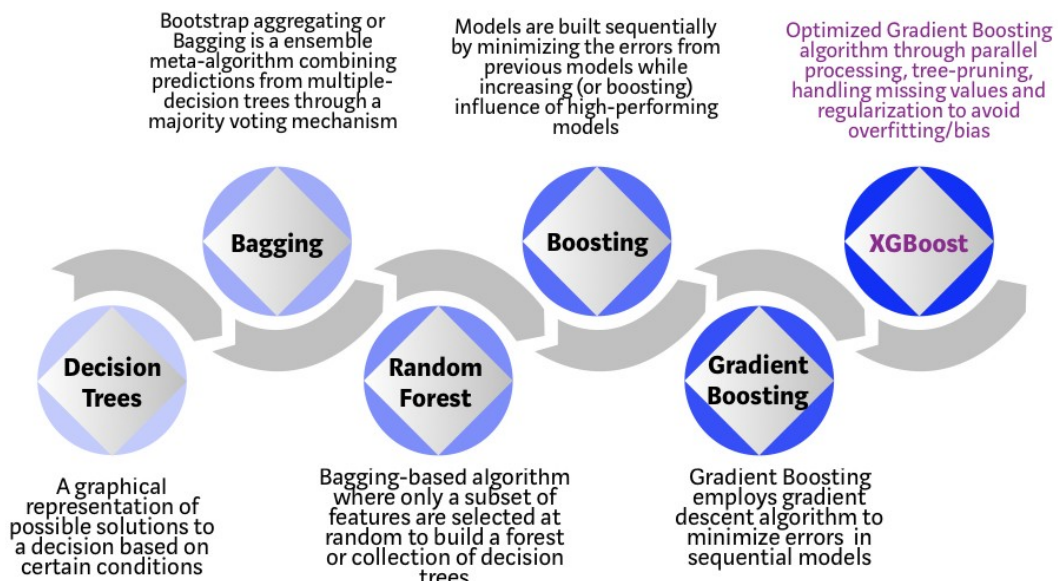


Figure 4.2: Evolution of XGBoost Algorithm from Decision Trees[24]

Each XGBoost model (and in general almost all ML models) have **hyperparameters** - parameters that describe the model itself (and have a big impact on its results). The most important ones, which will be changed in this work are (in xgboost version: 1.3.3)[25]:

- **max\_depth** (default value = 6) - Maximum depth of a tree. Increasing this value will make the model more complex and more likely to overfit
- **gamma** (default = 0) - Minimum loss reduction required to make a further partition on a leaf node of the tree. The larger gamma is, the more conservative the algorithm will be
- **alpha** ( default = 0) - A L1 regularization term on weights. Increasing this value will make the model more conservative

- **learning\_rate** (default = 0.3) - Step size shrinkage used in update to prevents overfitting.  
After each boosting step, we can directly get the weights of new features, and eta shrinks the feature weights to make the boosting process more conservative
- **n\_estimators** (default = 6) - Number of gradient boosted trees. Equivalent to number of boosting rounds

There are multiple ways to choose the optimal configuration (values) of hyperparameters, notably Grid Search, Random Search, and Bayesian Optimisation[26]. The comparison between them is shown in Table 4.1. Following the comparison and the method chosen earlier by the CBM-ML group[23], **Bayesian Optimisation** will be used in this work.

Table 4.1: Comparison of hyperparameters optimization methods

	<b>Grid Search</b>	<b>Random Search</b>	<b>Bayesian Optimisation</b>
Checks every configuration	+	-	-
Not much time needed to find the optimal configuration	-	+/-	+
Learns with each step	-	-	+



# Traditional methods of particles identification

## 5.1 Particle identification using the time-of-flight method

The time-of-flight method (TOF) allows us to differentiate between the groups of particles such as pions, kaons, and protons (positrons). Using the reconstructed:

- momentum ( $p$ ) and charge ( $q$ ) (from the **STS** and **MVD** detectors)
- time of flight ( $t$ ) and length of the track in the detector ( $L$ ) (from the **TOF** detector)

the mass-squared of a reconstructed particle can be calculated following the formula:

$$m^2 = \frac{p^2}{c^2} \cdot \frac{c^2 t^2}{L^2 - 1} \quad (5.1)$$

where  $c$  - velocity of light. Making a 2D plot, showing  $m^2$  on the  $y$ -axis, and  $p \cdot q$  on the  $x$ -axis, we receive a plot such as in Figure 5.1. To further differentiate between the groups of the particles, Gaussian functions can be fitted to the distributions. However, the last step is a non-trivial task, causing the majority of the inaccuracy. While several solutions to this problem exist, such as multidimensional fitting (using more reconstructed variables), the application of ML algorithms will be discussed in this work.

Other groups of particles such as e.g., muons and electrons, can also be reconstructed using the data from other detectors (respectively MUCH and RICH), but it goes beyond the scope of this thesis.

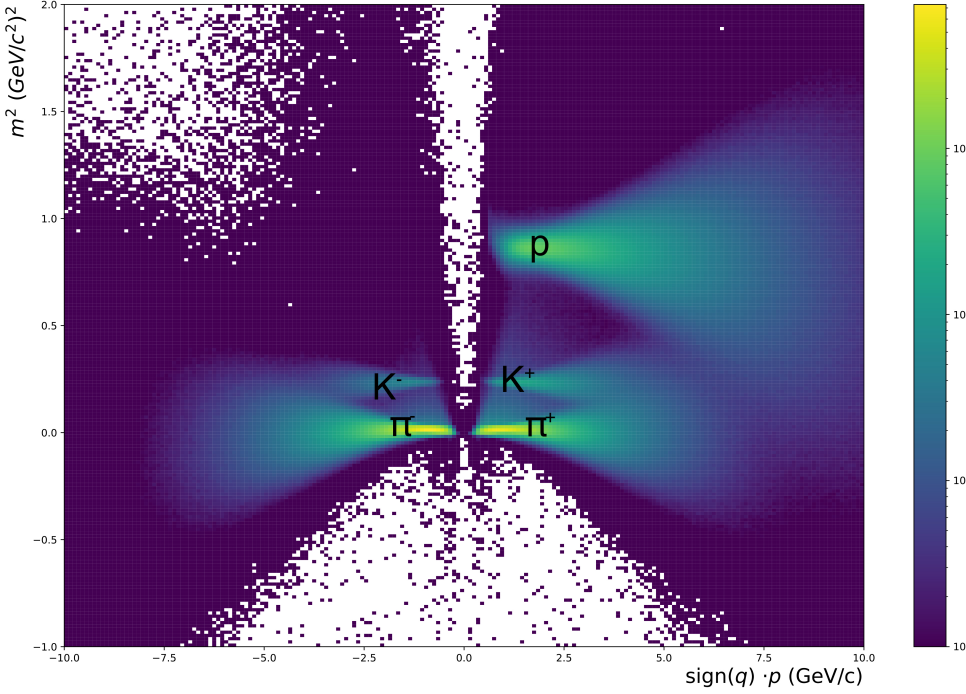


Figure 5.1: 2D TOF plot with pions, kaons, and protons shown

## 5.2 Short-lived particles reconstruction

Short-lived particles like  $\Lambda^0$ , and  $K_S^0$  have a neutral charge, therefore they cannot be detected directly using e.g., the TOF method. However, we can reconstruct these particles by investigating their *daughter particles* - particles coming from their decays. For example, in the main decay mode (66.7%) a K-short particle decays into a positive and negative pion (Figure 5.2). Using i.e. the STS, we can reconstruct the tracks of pions coming from this decay, and thus reconstruct the K-short particle.

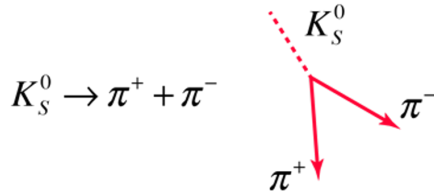


Figure 5.2:  $K_S^0$  main decay mode [28]

In order to do so, the **KFParticleFinder** was developed [29]. It is an on-line optimized reconstruction package based on Kalman Filter mathematics. It finds pairs of positive and negative pions (in the  $K_S^0$  case) which could be a result of the *mother* particle's decay.

### 5.2.1 PFSimple

For offline selection optimization and analysis, **PFSimple** package was created [30]. Using it, one can optimize selection criteria to differentiate between:

- **signal** - pion pairs created in K-short decay
- **background** - pions pairs returned by KFParticleFinder which are not the result of K-short decay

Also, PFSimple returns these attributes of each reconstructed particle:

- $L/\Delta L$  - distance between primary and secondary vertex divided over its error
- **DCA** - distance of closest approach between pion tracks
- $\chi^2_{\text{geo}}$  - dimensionless distance of closest approach between pion tracks
- $\chi^2_{\text{topo}}$  - dimensionless distance of closest approach between extrapolated kaon trajectory and primary vertex
- $\chi^2_{\text{prim}}$  - dimensionless distance between extrapolated secondary track and primary vertex
- $\cos(\alpha)$  - cosine of angle between pion and K-short momenta

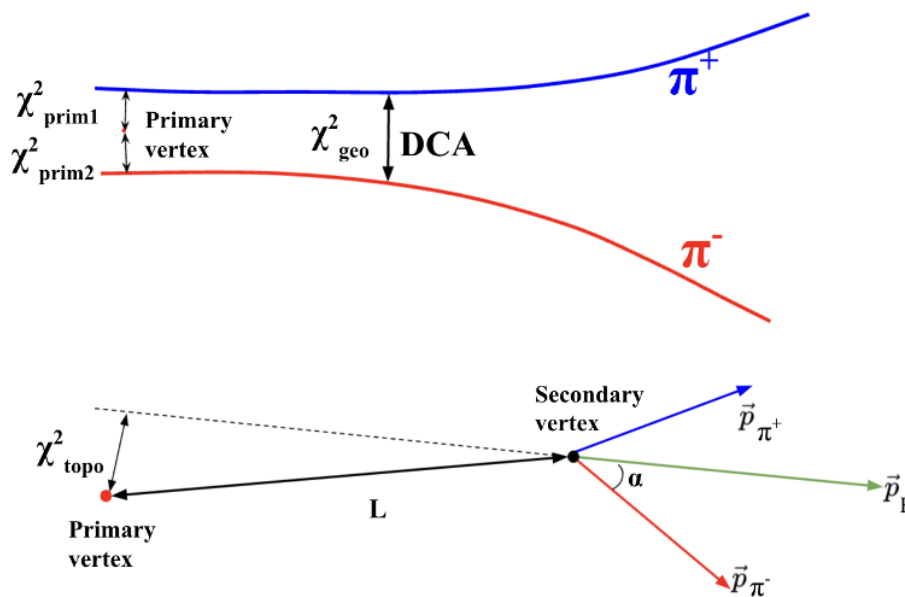


Figure 5.3: Decay scheme and topological variables of a  $K_S^0$  decay in the PFSimple

### Optimization of selection criteria

As the KFParticle Finder (and PFSimple) return all the possible pion pairs, which could be a result of K-short decay, some selection criteria need to be applied to differentiate between the signal and background.

We can also visualize manual selection criteria with a decision tree:

- For each variable of a reconstructed particle, a conditional statement is being set
- If all conditions are fulfilled, a K-short candidate is treated as a signal candidate

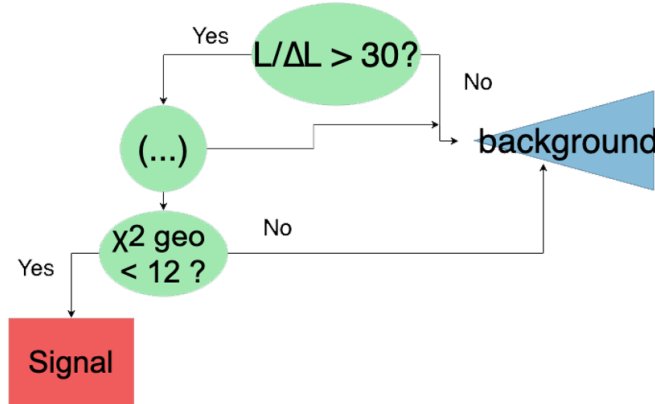


Figure 5.4: Example of a decision tree using manual selection criteria

The manual procedure for selection criteria optimization [30] is as follows:

1. The goal is to suppress as much background and to preserve as much signal as possible
2. Plot distribution of signal and background for some variable, and select a point above which all entries are considered as signal or background
3. Repeat it for all the variables

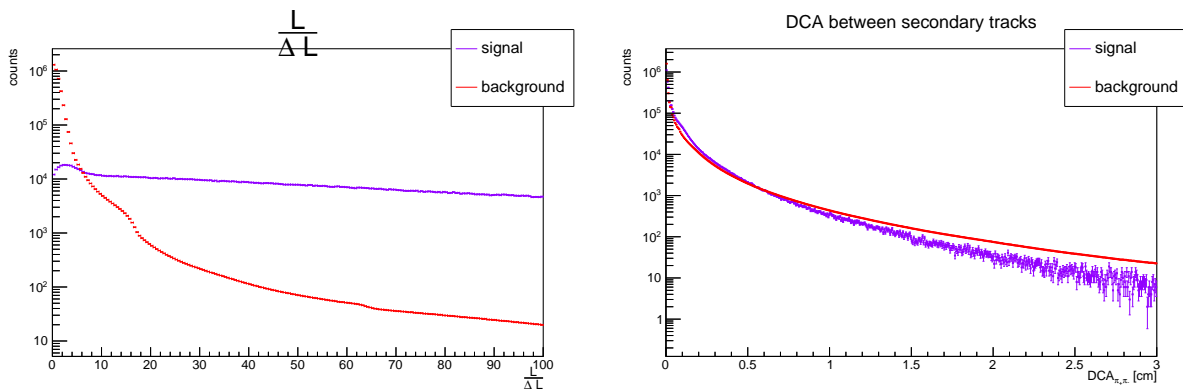


Figure 5.5: Example of distributions to be checked with the manual selection criteria optimization

However, this task is non-automatized (must be repeated for each particle), collision simulating model dependent, and only linear (as one variable at a time is used). In this work, the application of ML algorithm for the optimization of selection criteria will be discussed.

# Optimizing $K_S^0$ reconstruction using ML

In this chapter, the application of the ML algorithms for optimizing  $K_S^0$  reconstruction (and thus proper identification) will be discussed. As opposed to the traditional method mentioned in the chapter before, the predicted advantages and disadvantages are presented in the table below:

Table 6.1: Advantages and disadvantages of ML selection criteria optimization

Advantages	Disadvantages
Non-linear in multi-dimensional space	Not easily interpretable
Automatization of the selection process	Computationally expensive
Partially collision simulating model-independent With <i>probability</i> a value from which we consider a particle as a K-short particle can be chosen; it can aim for better reconstruction efficiency or a better background reduction	

The accuracy of these predictions will be checked in this chapter. The results of the K-short reconstruction optimization and have been presented before in [31] (some fragments of this report will be presented in the following sections).

## 6.1 Model preparation

All the data is stored in the AnalysisTree format, later passed through the PFSimple (C++ with ROOT framework), which returns all the possible K-short's daughter particles pairs, from which we could reconstruct a K-short particle. All the possible pairs along with the variables (described in the chapter before) are available for training in the *PlainTree* format, which can be loaded into Pandas Dataframe (Python), using a function prepared by the CBM-ML group[32]. Version 3.7 of Python was used, with the following libraries:

- pandas (version 1.3.4)
- xgboost (version 1.3.3)
- scikit-learn (version 1.0.1)
- bayesian-optimization (version 1.1.0)

The parts of the code used for the ML model training are shown in Appendix A.

### 6.1.1 Data enriching

There are two problems to tackle before providing datasets to our ML model: underrepresentation and dependence of collision simulation model.

#### Dependence of collision simulation model

To make the ML model partially independent of the collision simulation model, select:

- primary  $K_s$  candidates only in  $5\sigma$  region:  $0.43485 - 0.56135$  ( $\text{GeV}/c^2$ ) from DCM-QGSM-SMM model, (simulation data)
- background outside  $5\sigma$  region from UrQMD model, which mimics experimental data (will be replaced by real experimental data while CBM experiment starts)

Also, the UrQMD model is being used as a test dataset (as the model does not "know" the signal candidates from this MC model).

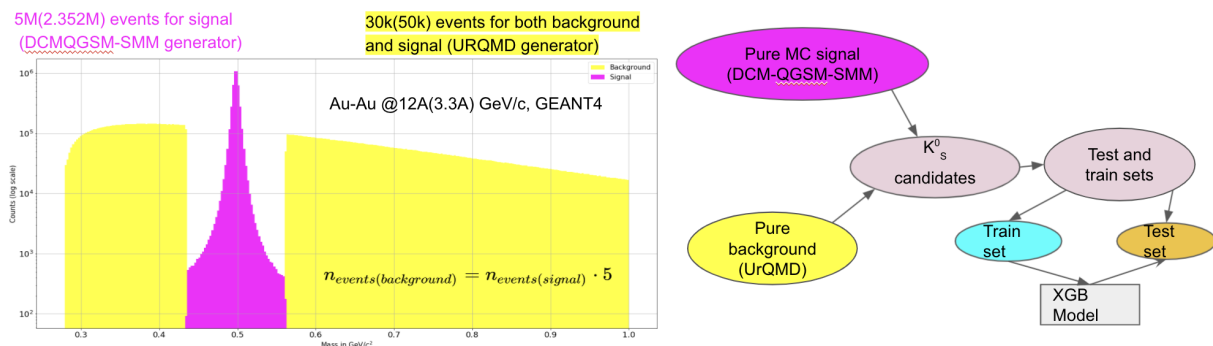


Figure 6.1: Data enriching

In total, the following datasets will be used:

- 5M (2.352M) events for signal generated in DCM-QGSM-SMM
- 30k(50k) events for both background and test dataset generated in UrQMD

Au-Au @12A(3.3A) GeV/c passed through CBM setup in GEANT4, and PFSimple.

#### Underrepresentation

As in the simulated data, less than 0.1% of  $K$ -short candidates are signal candidates, the ratio in the training dataset has to be changed so that the model learns how to identify signal candidates well. The number of background entries is rescaled by this formula:

$$n_{\text{events}(\text{background})} = 5 \cdot n_{\text{events}(\text{signal})} \quad (6.1)$$

### 6.1.2 Data cleaning

To reject the numeric values of parameters that do not have physical sense, but are present in the data set, some selection criteria are applied before the beginning of the model training. Similarly, some values which might be possible but are rare enough are rejected, to reduce the amount of data.

## Invariant mass

As the K-short particle decays into two pions, its invariant mass cannot be smaller than the mass of the two pions, so:

$$m_{\text{inv}} > 0.279 \text{ GeV}/c^2$$

Also, to reduce the amount of data:

$$m_{\text{inv}} < 1 \text{ GeV}/c^2$$

## Distances and $x, y, z$ coordinates

Distance between the primary vertex (the point where the collision of the nuclei happens), and the secondary vertex (the extrapolated point where the two daughter particles should have crossed each other) -  $l$  and the distance of closest approach between the two pions -  $DCA$  - should not be smaller than zero:

$$DCA, l, \frac{l}{\Delta l} > 0$$

Also, due to the sizes of the tracking system (the largest station has an area of  $1\text{m}^2$ ):

$$DCA < 100 \text{ cm}$$

For the same reason:

$$|x|, |y| < 50 \text{ cm}$$

As the particle has to hit 3 stations of the tracking system, and the last two are placed above 80 cm:

$$l < 80\text{cm}$$

For the same reason, and because of the fixed target geometry of the detector:

$$-1 \text{ cm} < z < 80 \text{ cm}$$

To reduce the data, we set:

$$\frac{l}{\Delta l} < 15000$$

However, in the KFParticle package  $l$  is assumed to be signed by design, and one can notice that actually, some data entries have a negative value of distance, for both signal and background. As the *quality cuts* should be rather conservative, the following ranges are set:

$$l > -5 \text{ (cm)}$$

$$\frac{l}{\Delta l} > -25$$

## Momentums

The fixed target geometry of the detector requires that:

$$p_Z > 0 \text{ GeV/c}$$

To reduce the data:

$$p < 20 \text{ GeV/c}; p_T < 3 \text{ GeV/c}$$

## Chi square

Since  $\chi^2$  is a squared distance, all the values must be larger than zero:

$$\chi^2 > 0$$

To reduce the data, following the maximal values are selected:

- $\chi^2$  first and second  $< 3 \cdot 10^7$
- $\chi_{geo}^2 < 10000$
- $\chi_{topo}^2 < 100000$

## Pseudorapidity

As pseudorapidity depends on the polar angle as

$$\eta = -\ln \tan\left(\frac{\theta}{2}\right) \quad (6.2)$$

where  $\theta$  - polar angle, and the STS covers the polar angles between  $2.5^\circ$  and  $25^\circ$ , for which the pseudorapidity values would equal:

$$1.5 < \eta < 3.82$$

However, due to the magnetic field, the pseudorapidity is constrained to the following values:

$$1.0 < \eta < 6.5$$

with which 0.06% of data for signal is lost (instead of 5.66%) and 0.08% of data for background (instead of 6.75%)

### 6.1.3 Variables selection

The last step before training our model is the selection of variables that will be used in the training of the discriminator. To make the model simpler, there is no need to use two variables if they are strongly correlated with each other. Also, to avoid signal/background classification directly by invariant mass, variables strongly correlated with the invariant mass of background should be omitted.

## Correlation matrix

The Pearson correlation efficient of each variable is being calculated following this formula:

$$\rho = \frac{\text{COV}(X, Y)}{\sigma_X \times \sigma_Y} \quad (6.3)$$

where:

$$\text{COV}(X, Y) = E[(X - E[X])(Y - E[Y])] \quad (6.4)$$

$$\sigma_X = \sqrt{E[(X - E[X])^2]} \quad (6.5)$$

They are then plotted in a matrix:

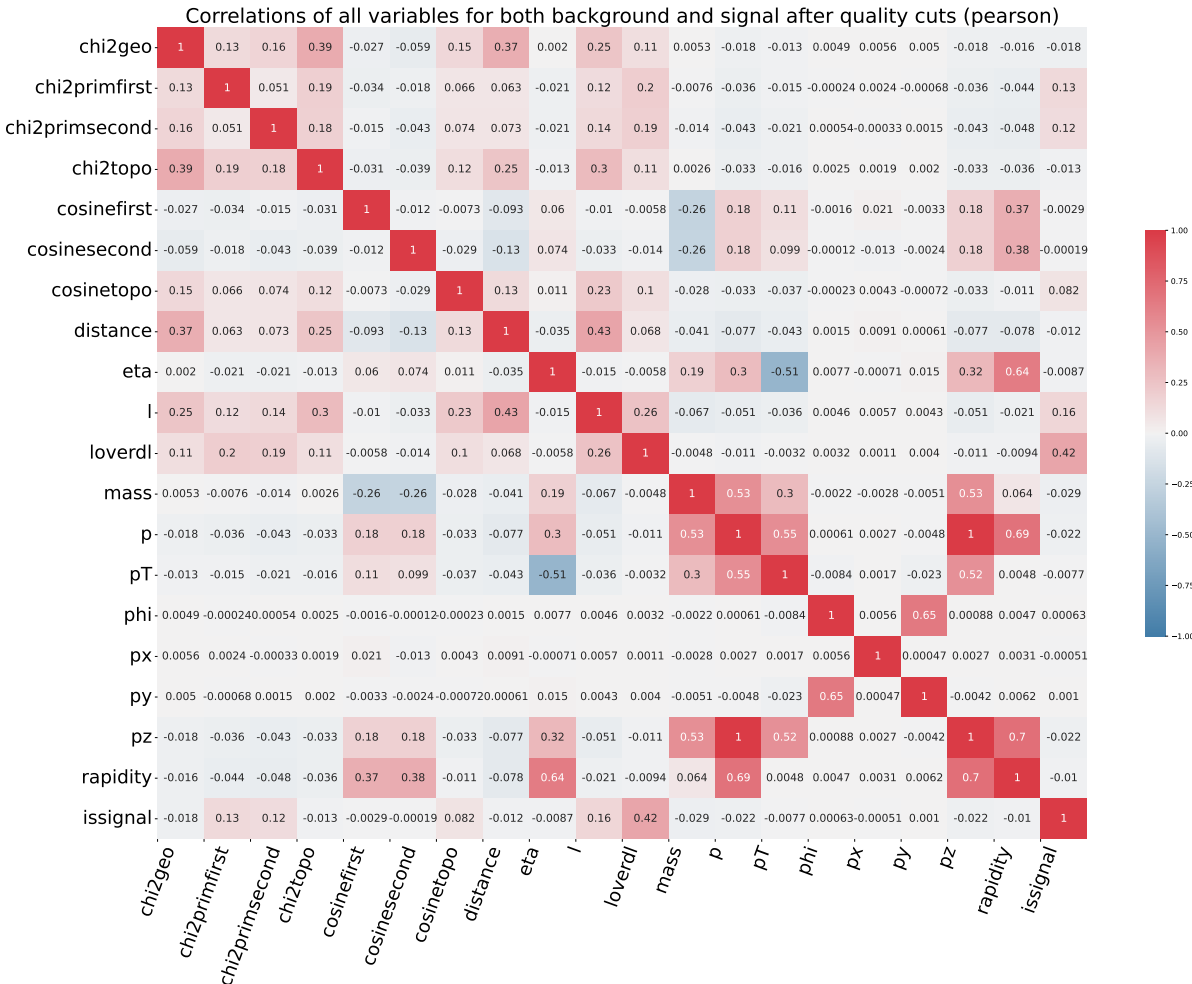


Figure 6.2: Correlation matrix

## Correlation with invariant mass

Later, the correlation (Pearson coefficient) of each variable with the invariant mass of (separately) signal and background is being checked

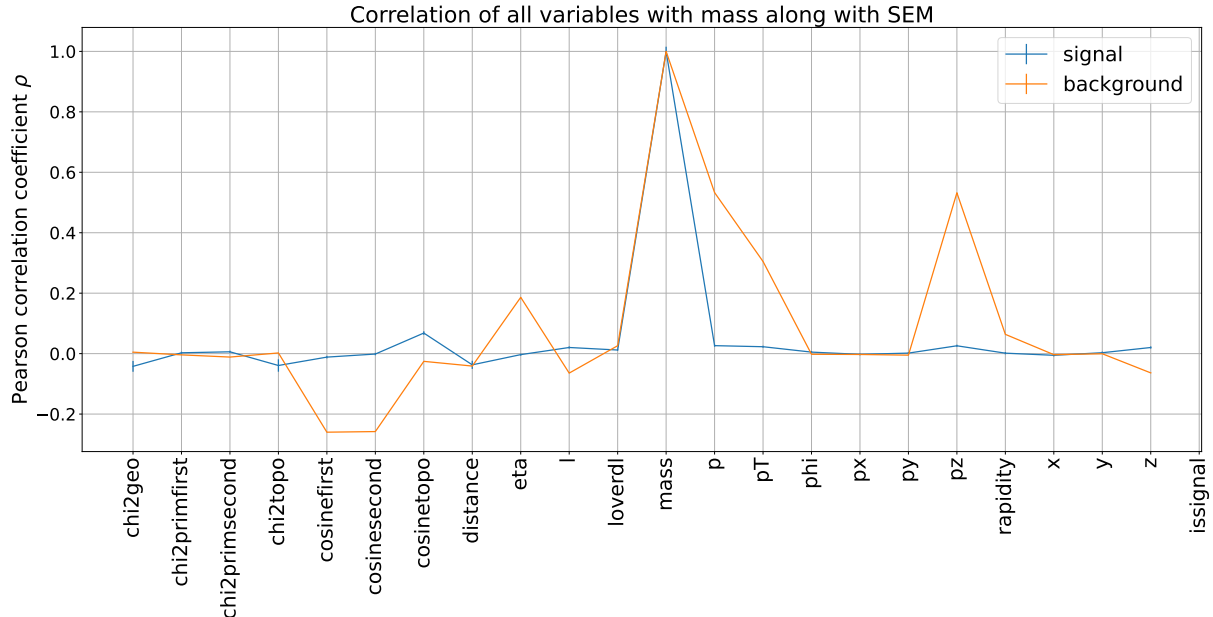


Figure 6.3: Correlation of all variables with mass

## Selected variables

Based on that, the following 6 variables are selected for the training:  $L/\Delta L$ ,  $DCA$ ;  $\chi^2_{geo}$ ,  $\chi^2_{topo}$ ,  $\chi^2_{primfirst}$ ,  $\chi^2_{primsecond}$

## 6.2 Model training

### 6.2.1 Results for $p_{beam} = 12\text{A GeV}/c$

Having prepared the data, the training of the ML algorithm may be initiated. To choose the hyper-parameters of the XGBoost model, the Bayesian Optimisation package was used.

## Cross-validation

To check if the model works as well on new data, as on the training dataset, Receiver Operating Characteristic and probability plots are drawn.

Receiver Operating Characteristic illustrates the diagnostic ability of a binary classifier. Threshold on the ROC (Receiver Operating Characteristic) curve which maximizes Approximate Median Significance

$$AMS = \sqrt{2}[(tpr + fpr) \log(1 + tpr/fpr) - tpr] \quad (6.6)$$

(where  $t(f)pr$  is true (false) positive rate) on the test sample is the best threshold.

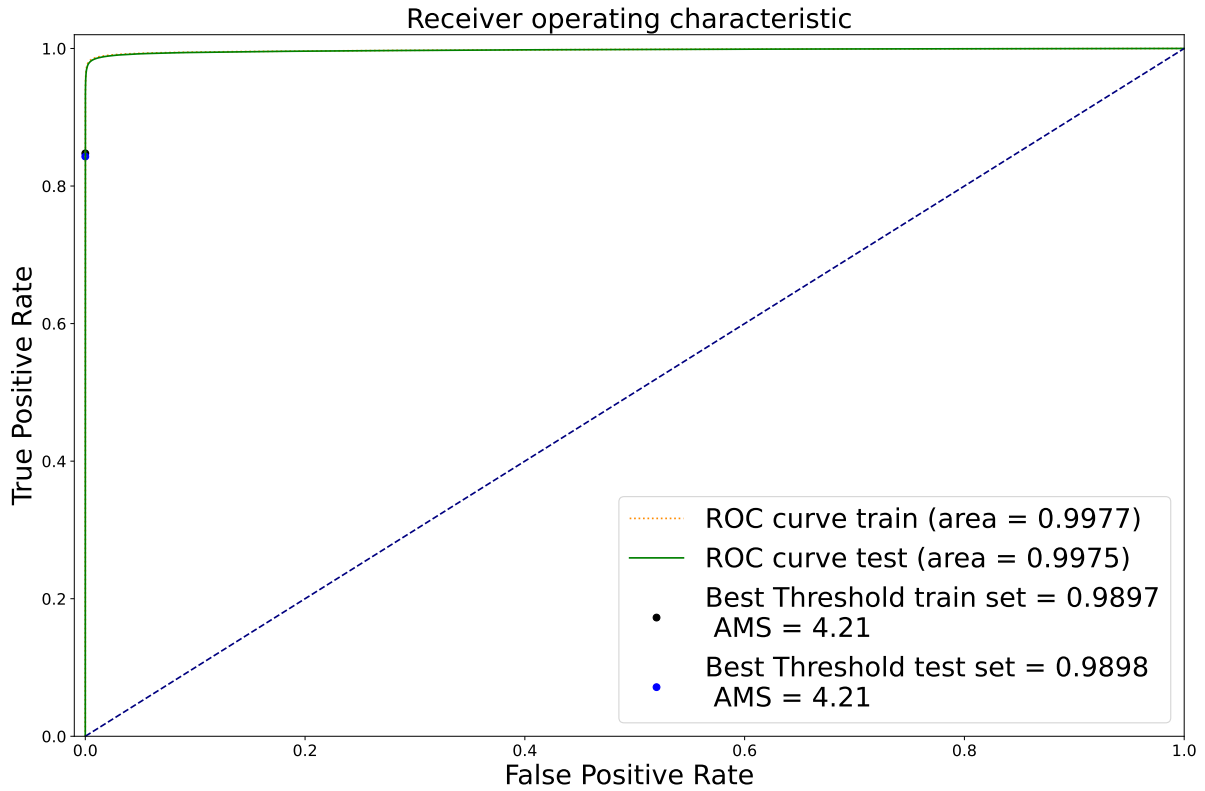


Figure 6.4: Receiver Operating Characteristic

We see that the optimal point on ROC is similar for both train and test datasets. The graph of signal/background share in both train and test datasets is also plotted.

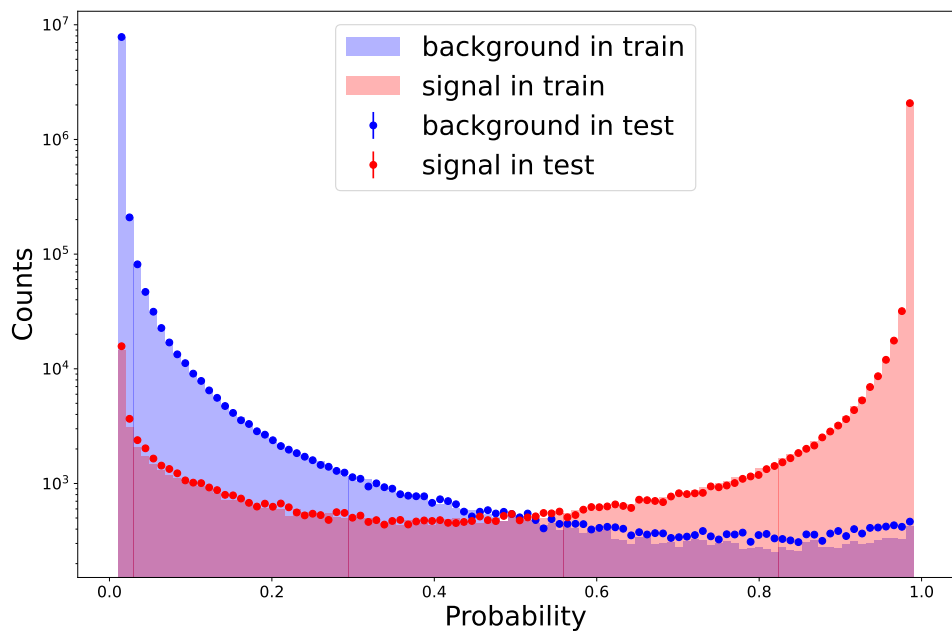


Figure 6.5: Probability plot

Once again, the results are similar for the two datasets. Hence, we can say that our model is not overtrained (works well on new data).

The invariant mass distribution before and after XGB selection is presented below:

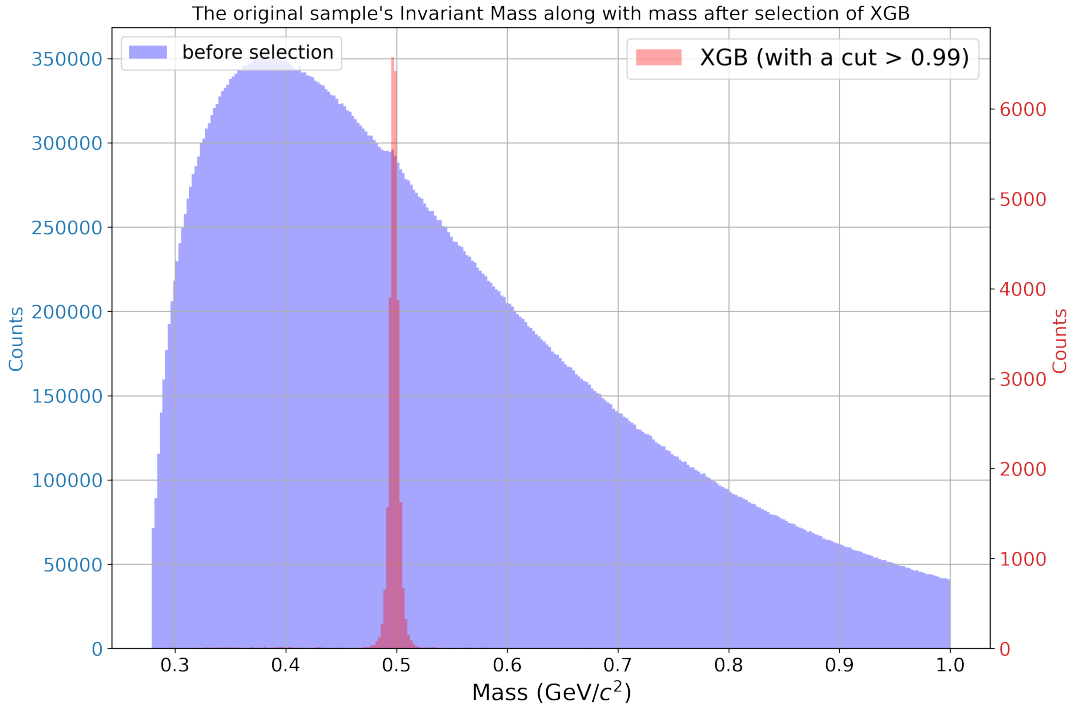


Figure 6.6: Invariant mass distribution

### Comparison with default KFPF Cuts

KFParticleFinder has default selection criteria, which can be compared with ML selection:

- $L/\Delta L > 5$
- $DCA < 1 \text{ cm}$
- $\chi^2_{geo} < 3$
- $\chi^2_{prim} > 18.4$
- $\cos(\alpha) > 0$

Depending on the cut value, better background reduction or better efficiency can be obtained.

With a cut value set to 0.99, we get  $50\times$  less background (Fig. 6.7):

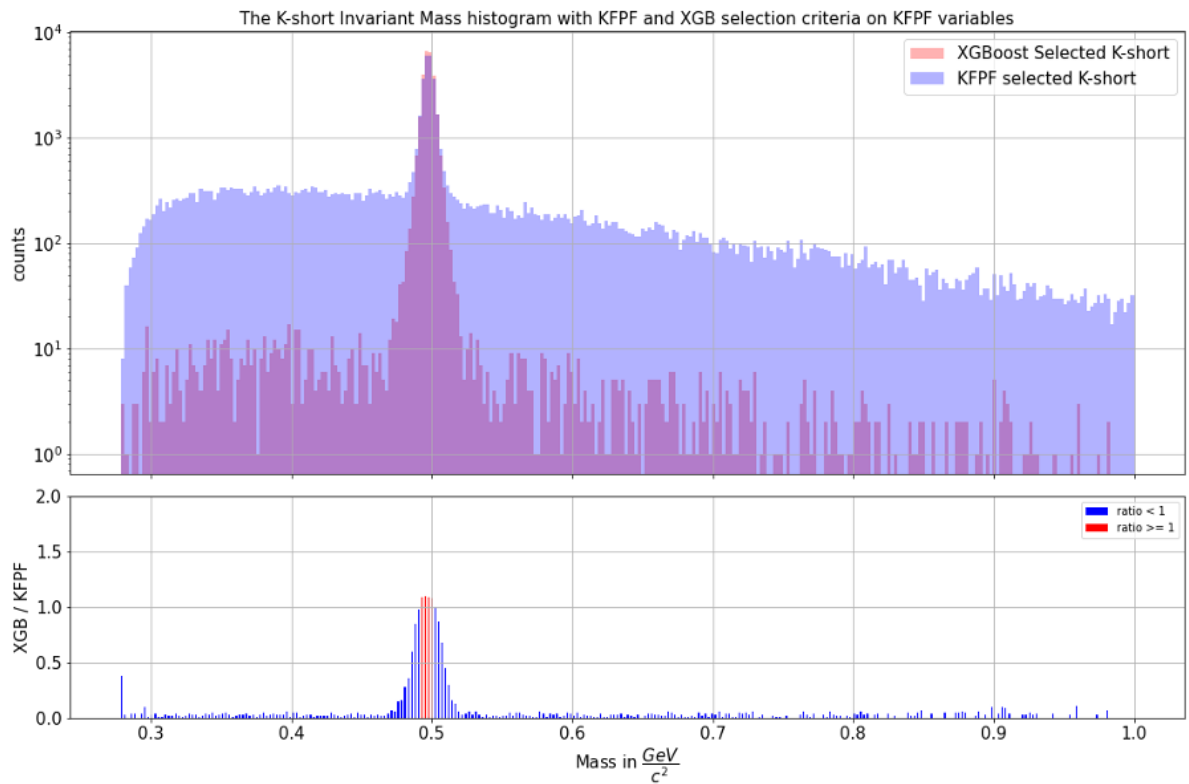
- **Reconstructed  $K_S^0$ /reconstructible  $K_S^0 = 80.67\%$**  vs. 76.93% with default KFPF cuts
- **false / true positive rate = 0.04** vs. 2.01 with default KFPF cuts

With a cut value set to 0.86, we get 20% better efficiency (Fig. 6.8):

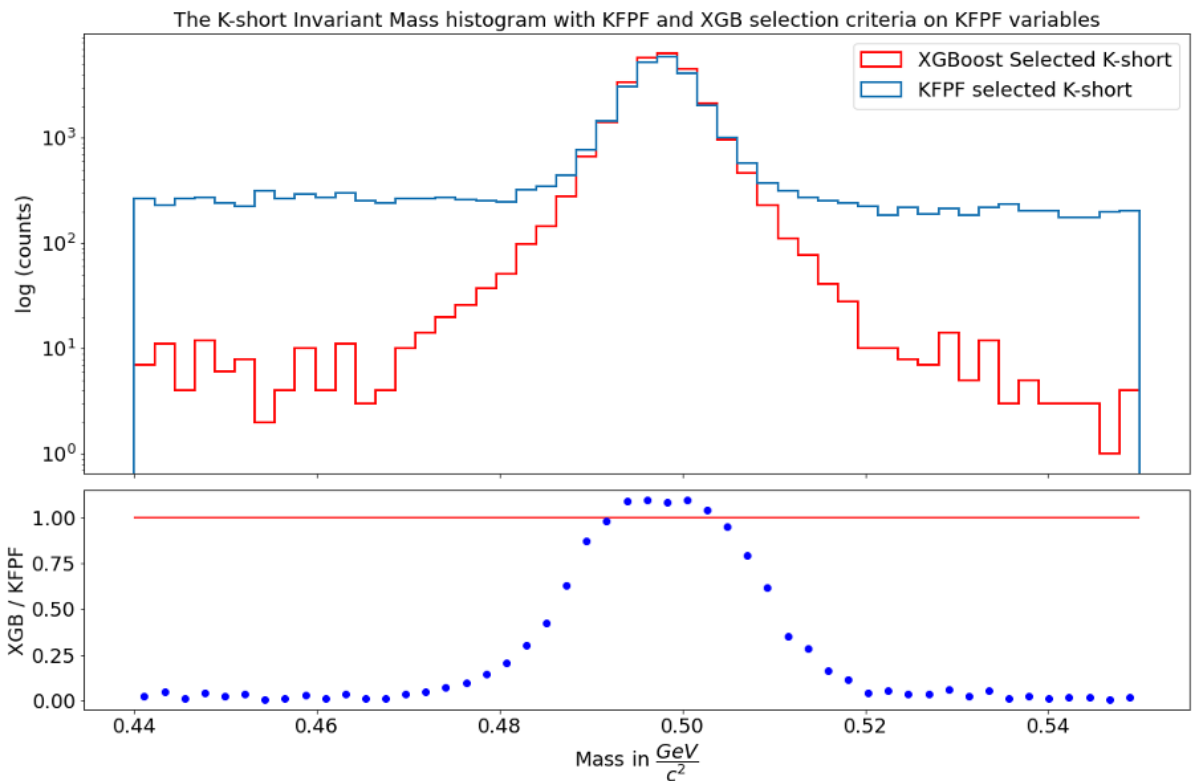
- **Reconstructed  $K_S^0$ /reconstructible  $K_S^0 = 95.91\%$**  vs. 76.93% with default KFPF cuts
- **false / true positive rate = 1.27** vs. 2.01 with default KFPF cuts

### Investigation of potential bias

To check if the XGB selection criteria cut tails of the distribution, or are biased in some regions, the invariant mass distribution of true and false positives is plotted (Figure. 6.9). We see that

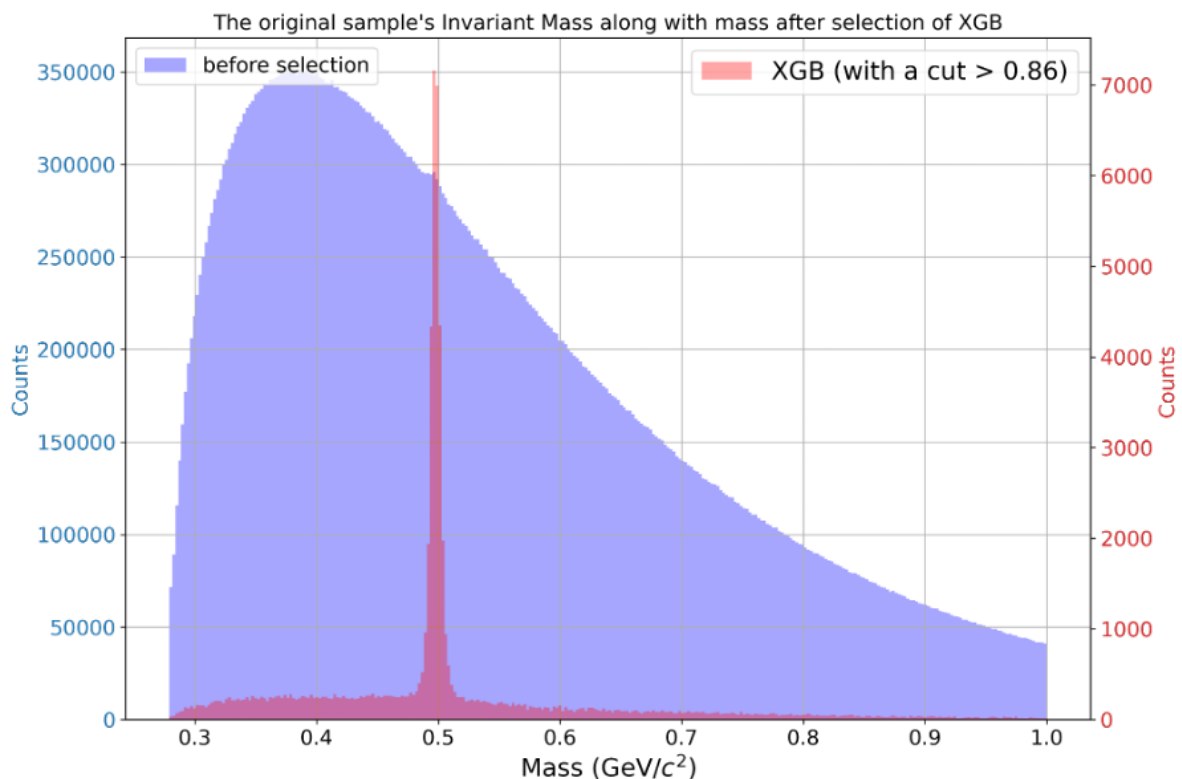


(a) Invariant mass distribution (y log scale)

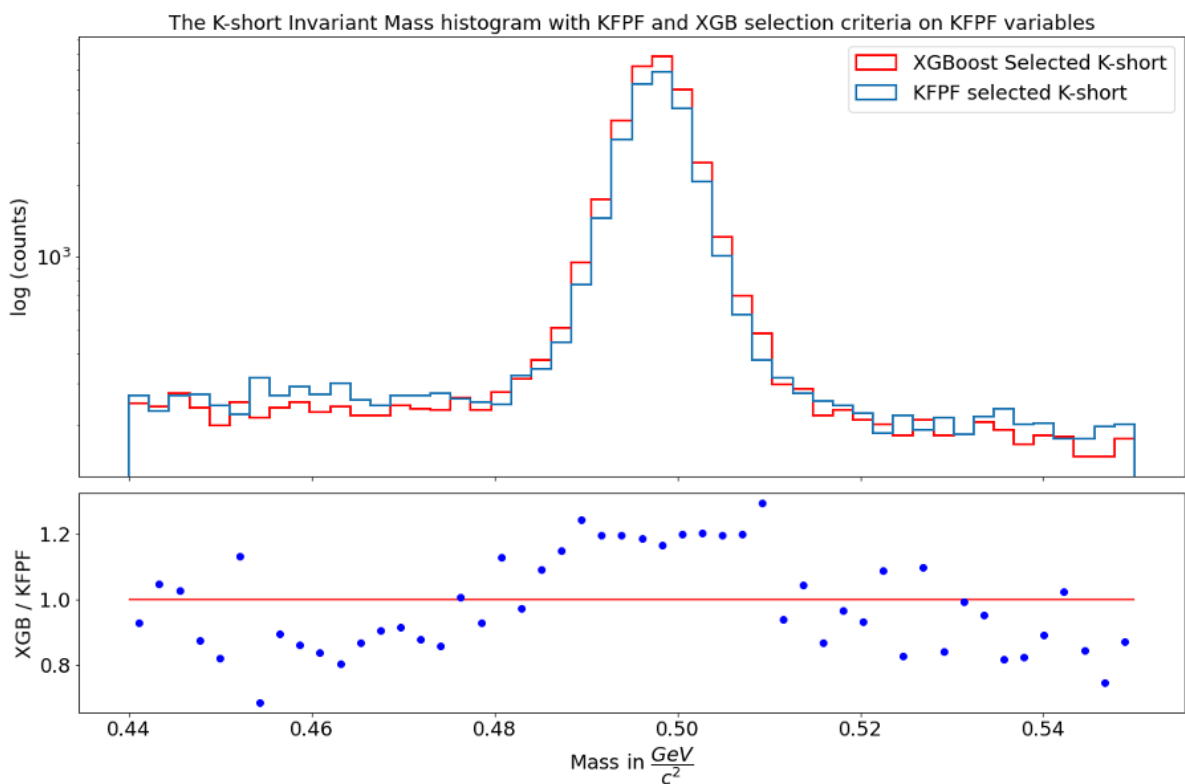


(b) Invariant mass distribution (close-up)

Figure 6.7: Comparison with KFPF cuts

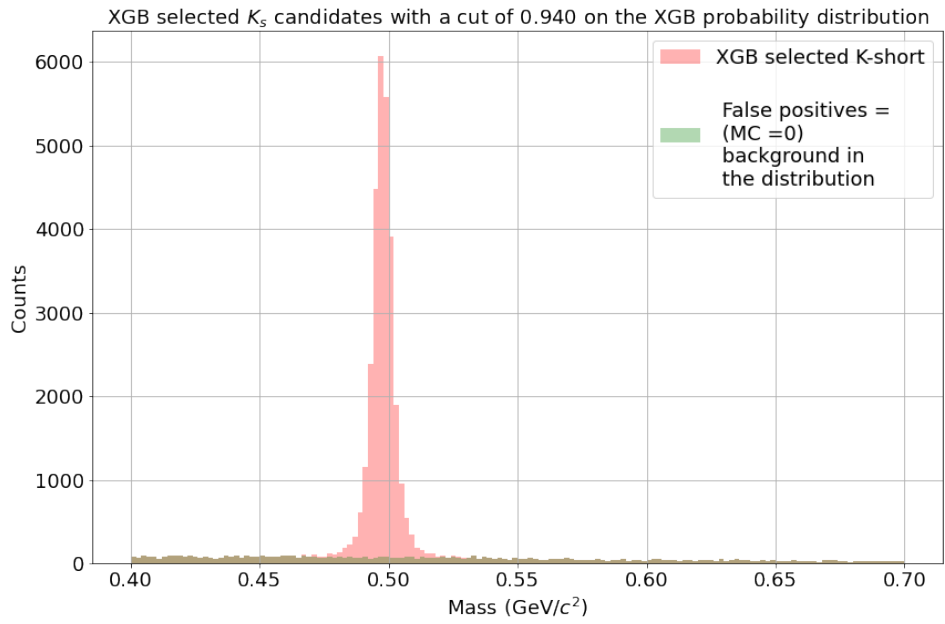


(a) Invariant mass distribution (y log scale)

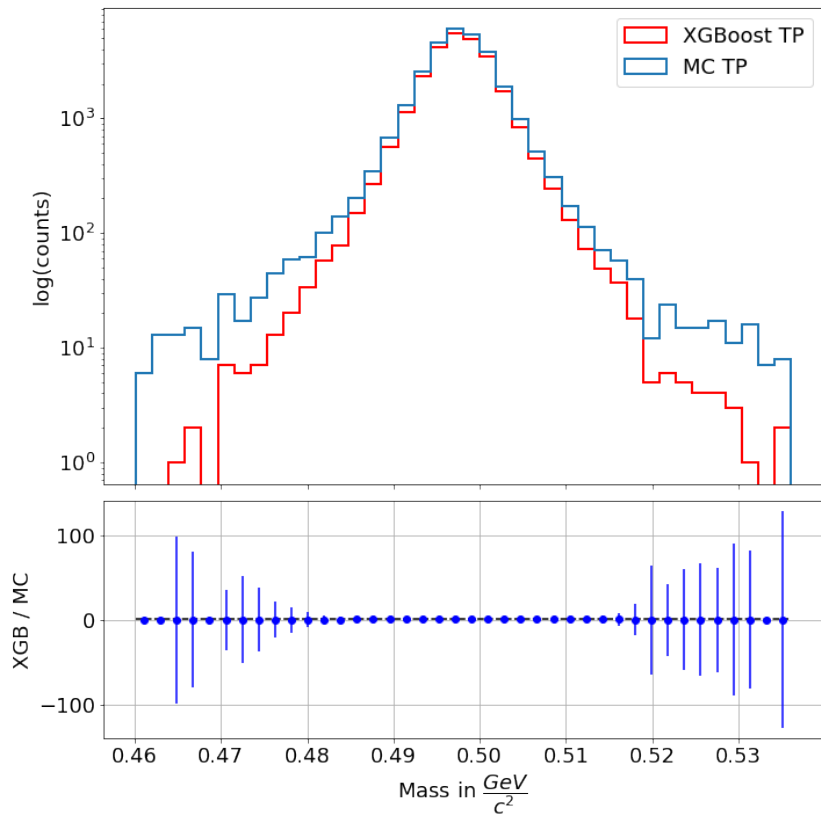


(b) Invariant mass distribution (close-up) - comparison with KFPF cuts

Figure 6.8: Invariant mass distribution for probability  $> 0.86$



(a) Selected  $K_S^0$  and false positives distribution



(b) Reconstructed and MC true positives (y log scale)

Figure 6.9: True-false positives investigation

our model does not seem to be biased towards any invariant mass region.

## 6.2.2 Results for $p_{\text{beam}} = 3.3\text{A GeV/c}$

### Comparison with KFPF cuts

The same code can be used to obtain similar results for another CBM energy level. Comparing to default KFPF cuts, with probability cut 0.9635 (Fig. 6.10):

- **Reconstructed  $K_S^0$ /reconstructible  $K_S^0 = 93.45\%$**  vs. 78.94% with default KFPF cuts
- **false / true positive rate = 0.19** vs. 1.38 with default KFPF cuts

Due to the smaller statistics for this energy level, the ML model training should be redone for a bigger dataset.

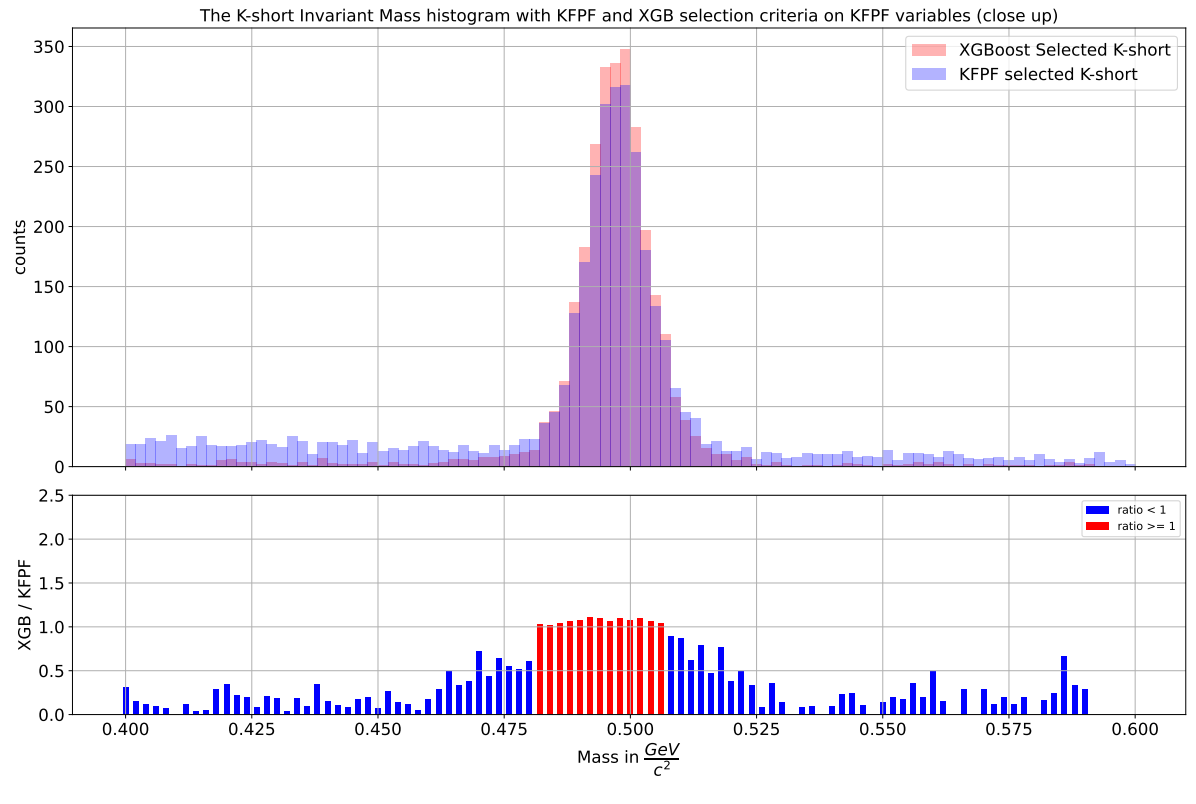
## 6.2.3 Influence of the magnetic field scaling

Obtained ML model can be adapted for the investigation of the influence of the magnetic field scaling. We compare: 100% MF strength (for  $p_{\text{beam}} = 12\text{A GeV/c}$ ), 56% and 27.5% MF strength (for  $p_{\text{beam}} = 3.3\text{A GeV/c}$ , both with only DCM generated data for 0.4M events for training and 0.1M for validation). We see (Fig. 6.11) that the stronger the magnetic field is, the broader  $K_S^0$  invariant mass distribution peak is. Also, we observe much more signal entries for  $p_{\text{beam}} = 12\text{A GeV/c}$  (for the same number of events).

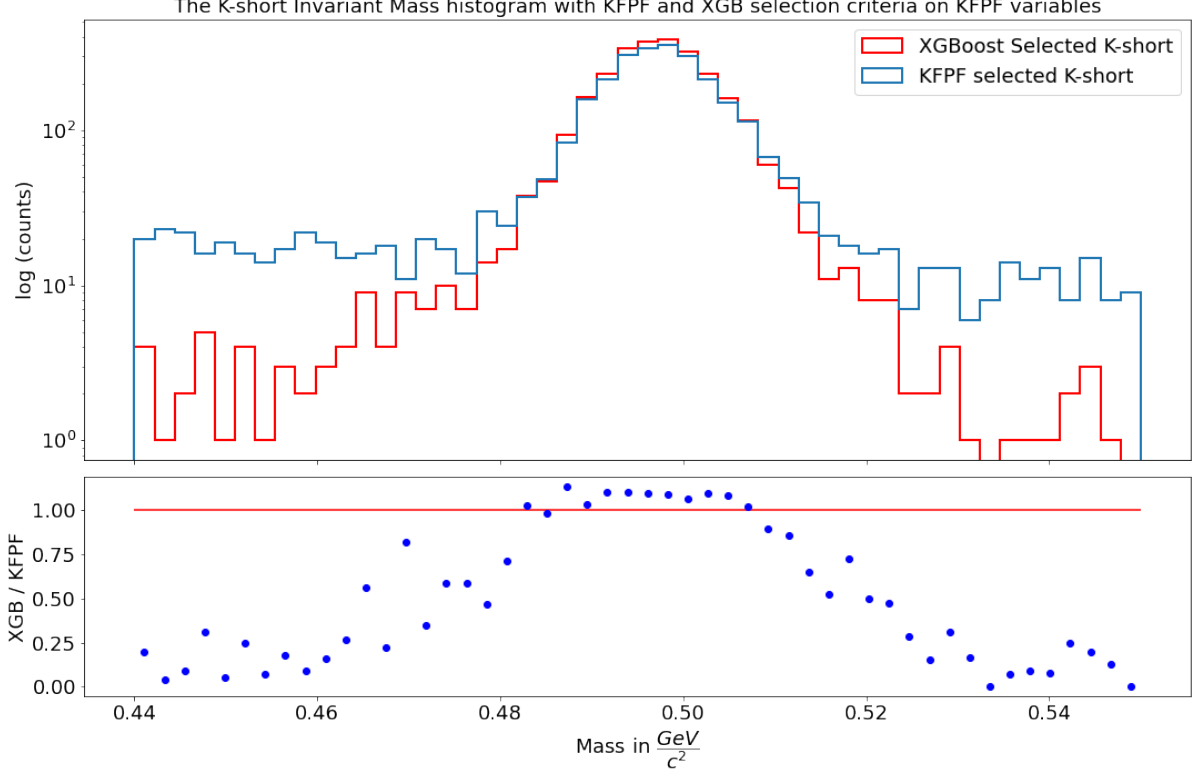
For  $p_{\text{beam}} = 3.3\text{A GeV/c}$  the number of signal entries is almost the same; we select the probability cut so that the false/true positive ratio is the same for both % of MF and compare the efficiency of the reconstruction (Tab. 6.2). We see that weaker MF does not necessarily worsen efficiency (only 2% difference). However, this comparison should also be redone for a bigger dataset.

Table 6.2: Comparison of MF strength vs. efficiency

ratio	12 A GeV/c MF=100%	3.3 A GeV/c MF=56%	3.3 A GeV/c MF=27.5%
reconstructed/reconstructible	89.98%	90.36%	88.49%
false / true positive	0.2	0.2	0.2



(a) Invariant mass distribution (y log scale)



(b) Invariant mass distribution (close-up)

Figure 6.10: Comparison with KFPF cuts for 3.3A GeV/c

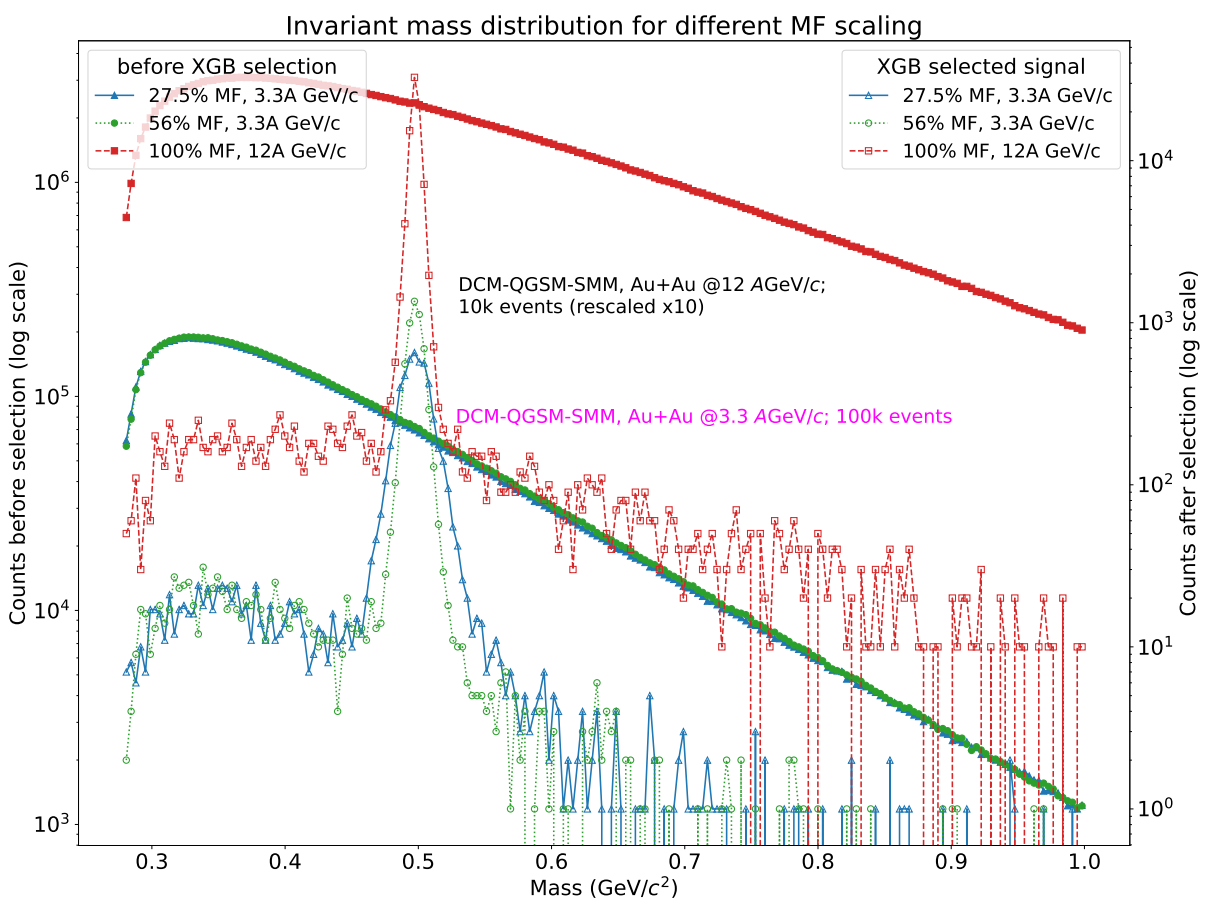


Figure 6.11: Invariant mass distribution for different MF scaling

# ”TOF” particles identification using ML

In this chapter, the application of the ML algorithms for particles identification (as the equivalent of the TOF method) will be discussed. As opposed to the traditional TOF method, instead of plotting mass-squared and  $p \cdot q$ , and then fitting Gaussians to the distributions to differentiate between the particles group, the data from MVD+STS and TOF detectors will be provided directly to the ML model. The aim is to differentiate between the three groups of particles:

- protons
- kaons
- pions (in the third group, the muons and electrons are included as well, as their mass-squared is almost indistinguishable without the data from other detectors)

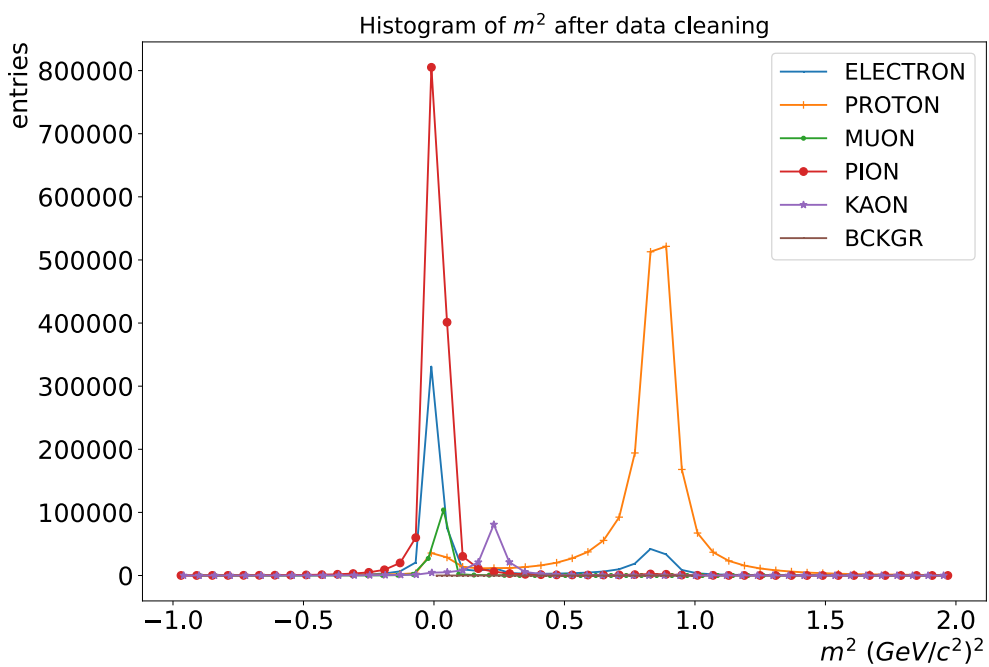


Figure 7.1: Histograms of mass-squared of each particle class (differences of quantity of each particle type can also be observed)

## 7.1 Model preparation

In this chapter, the data from the detectors saved in the AnalysisTree format is converted into a PlainTree format using a C++ program with ROOT libraries. Its fragments are presented in the appendix B. The following variables can be used:

- From MVD+STS: charge sign ( $q$ ); momentum components:  $p, p_T, p_x, p_y, p_z$ ; rapidity and pseudorapidity ( $\eta$ ); azimuthal angle ( $\phi$ )
- From TOF: mass-squared ( $m^2$ ), calculated by formula 5.1 (using  $p$  value from MVD+STS)
- From MC model: invariant mass; PID code, which returns the information about the type of particle in the PDG convention, e.g., -2212 = (-)anti—(2212)proton[33]

The same libraries were used as in chapter 6. For training and validation, the following datasets are used:

- 2M events generated in DCM-QGSM-SMM (training dataset)
- 1M events generated in UrQMD (test dataset)

Au-Au @12A GeV/c passed through CBM setup in GEANT4, and PFSimple. The different models used for training and validation allow us to check if the ML model is not biased towards a specific MC model.

### 7.1.1 Data enriching

#### Remapping

The four different classes will be loaded into the ML model:

- 0: protons
- 1: kaons
- 2: pions (with the muons and electrons)
- 3: *background* - all the other particles

The classes 0-2 are loaded into the model during the training. Later, if the probability returned by the XGB is smaller than a specific threshold, the particle is identified as 3 - background.

#### Underrepresentation

As different classes have a different number of particles, they are rescaled so that each class has the same number of elements (in this case, it is specified by the number of Kaons, as they are the most underrepresented class).

### 7.1.2 Data cleaning

To reject the numeric values of parameters that do not have physical sense, but are present in the data set, some selection criteria are applied before the beginning of the model training. As in chapter 6, some values which might be possible but are rare enough are rejected, to reduce the amount of data.

## Mass-squared

To constraint the mass-squared region to the one of the selected classes:

$$-1 < m^2 < 2 \text{ (GeV/c}^2)^2$$

Later during the training (not for the validation dataset), the mass-squared of each class will be constrained to a specific value of  $\sigma$  - standard deviation (6.5) around its mean value. After some tests, the following values were chosen:  $1\sigma$  region for ID=0 and ID=2;  $1.5\sigma$  for kaons (ID=1)

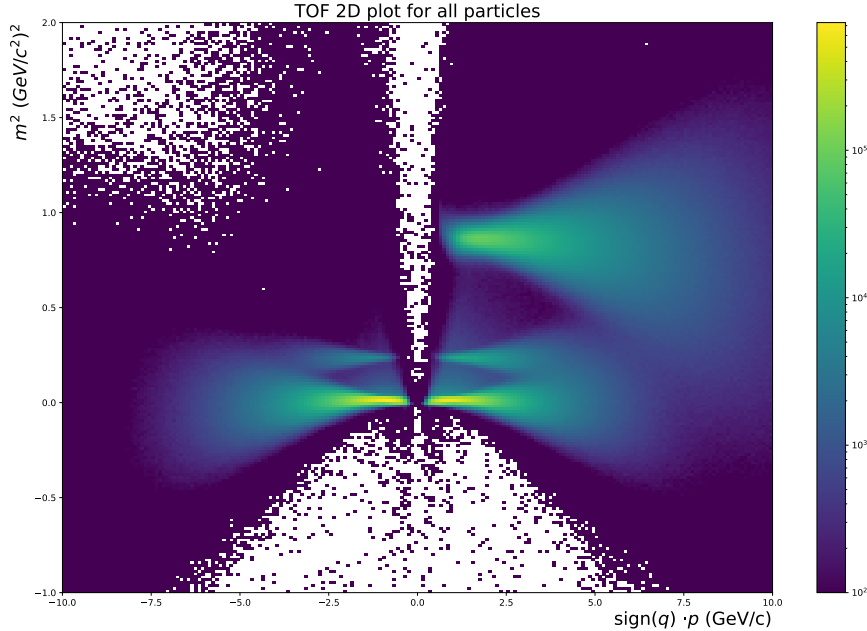


Figure 7.2: 2D TOF histogram of all particles after data cleaning

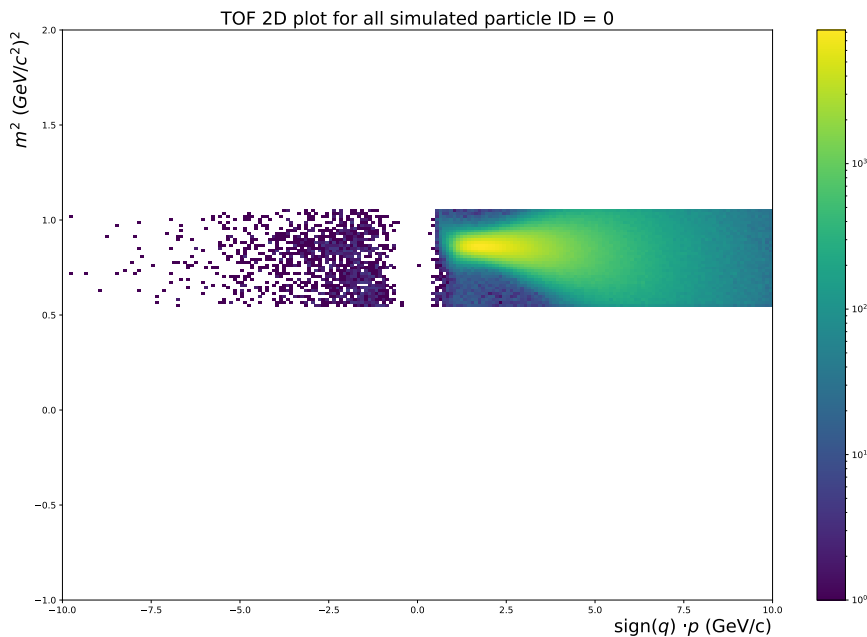


Figure 7.3: 2D TOF histogram of protons (ID=0) after  $1\sigma$  selection

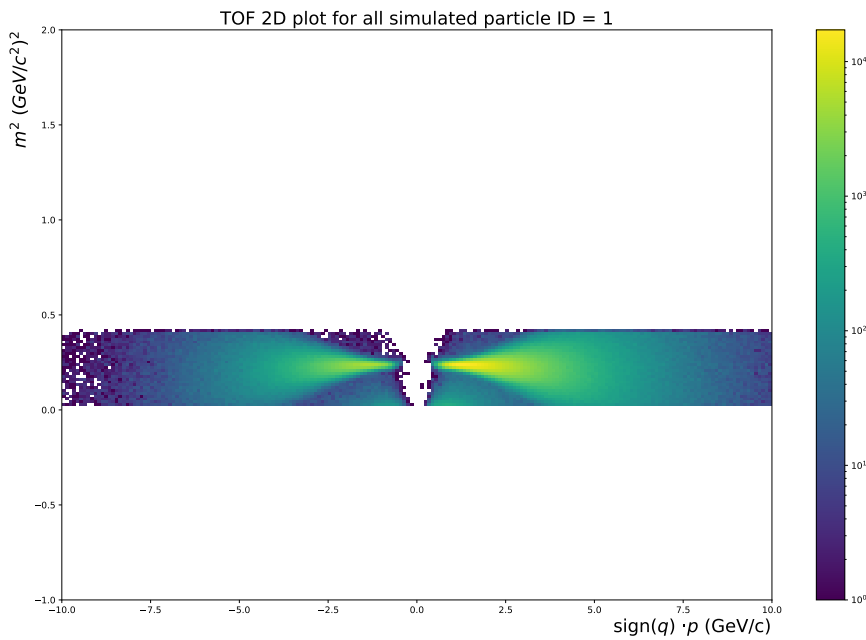


Figure 7.4: 2D TOF histogram of kaons (ID=1) after  $1.5\sigma$  selection

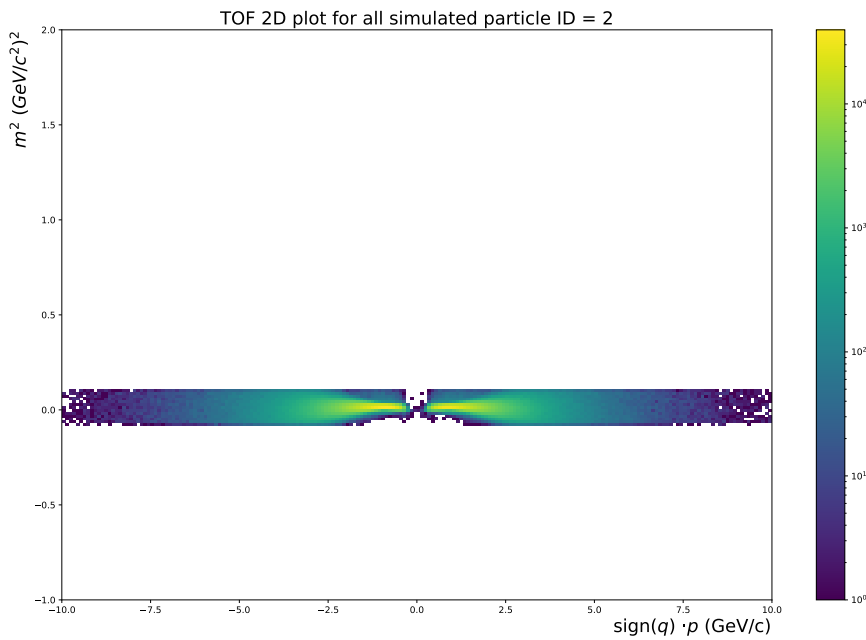


Figure 7.5: 2D TOF histogram of pions, muons and electrons (ID=2) after  $1\sigma$  selection

## Momentums

The fixed target geometry of the detector requires that:

$$p_Z > 0 \text{ GeV/c}$$

To reduce the data:

$$p < 12 \text{ GeV/c}; p_T < 2 \text{ GeV/c}$$

### 7.1.3 Variables selection

In this chapter, the TOF identification method is recreating, so the  $m^2$ ,  $p$  and  $q$  values are being used. However, the results coming from only those 2 values were not perfect (usually, it is better to train an XGBoost model using multiple variables). After plotting the correlation matrix (Figure 7.6), and following the other works[27], the  $p_T$  and  $\eta$  values are being selected also.

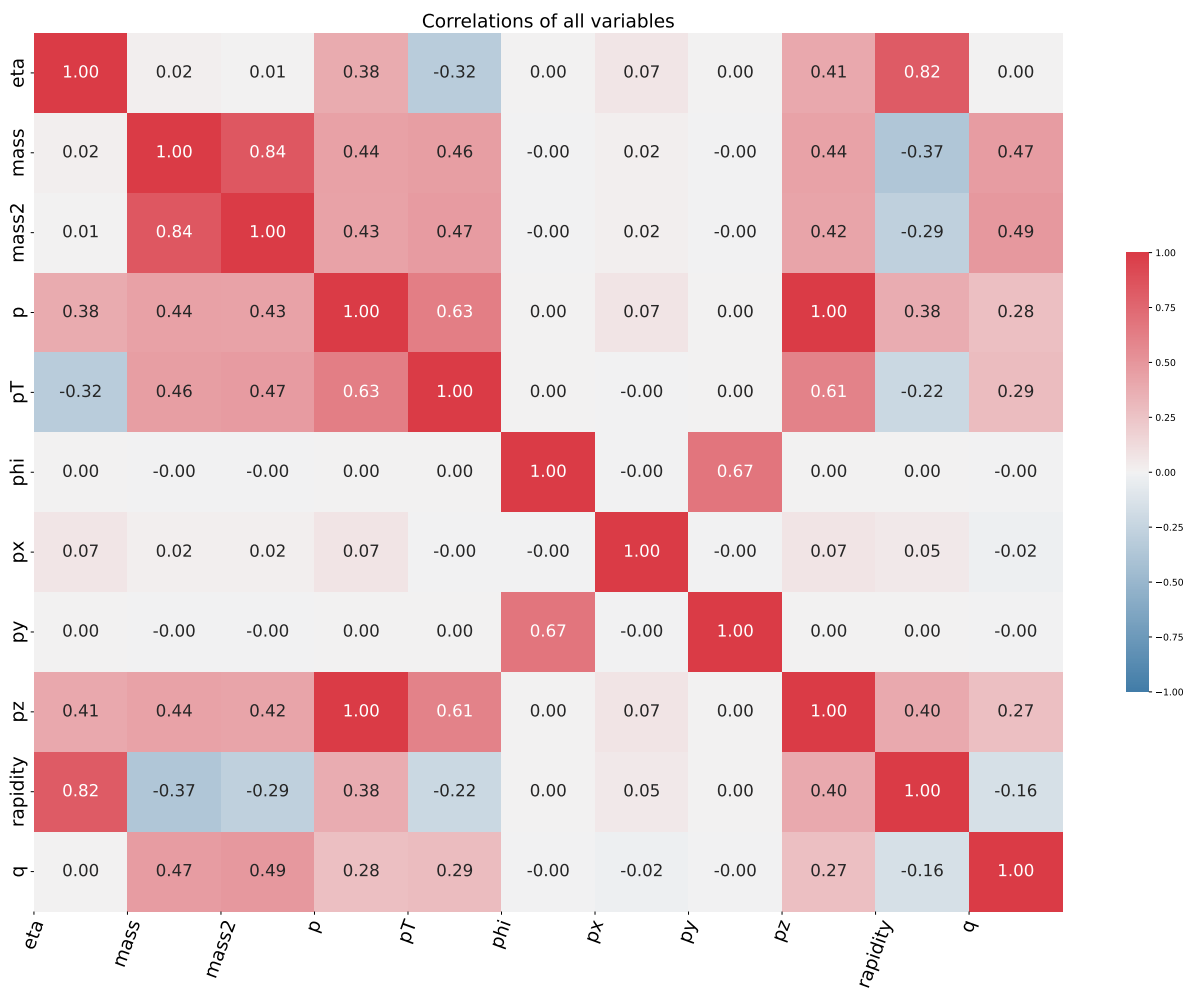


Figure 7.6: Correlation matrix

## 7.2 Model training

With the prepared data, the ML model training can be started. Once again, the hyperparameters are being selected using Bayesian Optimisation.

### 7.2.1 Probability plots

This time (contrary to K-short reconstruction optimisation), our model is a multi-class classifier (non-binary). For each particle, it returns the probability of belonging to each (0-2) class. The probability plot for all the classes can be plotted:

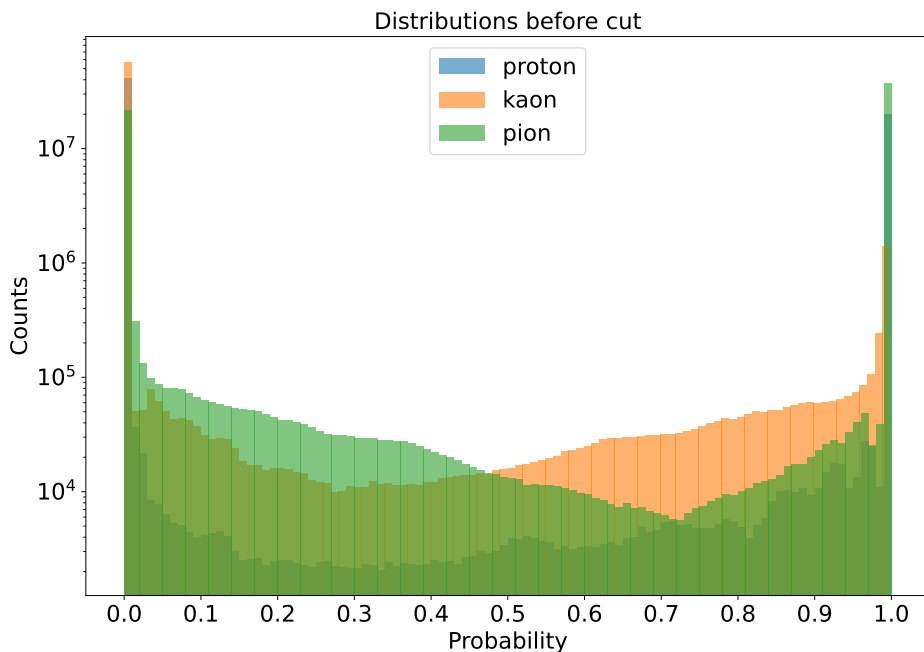


Figure 7.7: Probabilities distribution for all the classes

Later, the probability plot for each class can also be made, showing probability for all the particle vs. true-positives (particles belonging to the class). It allows to set a certain threshold, below which it is better to classify a particle as background (ID=3). With this approach, the number of false-positives is smaller; it also includes particles which don't belong to the 0-2 classes (e.g.,  $\Sigma^\pm$ ):

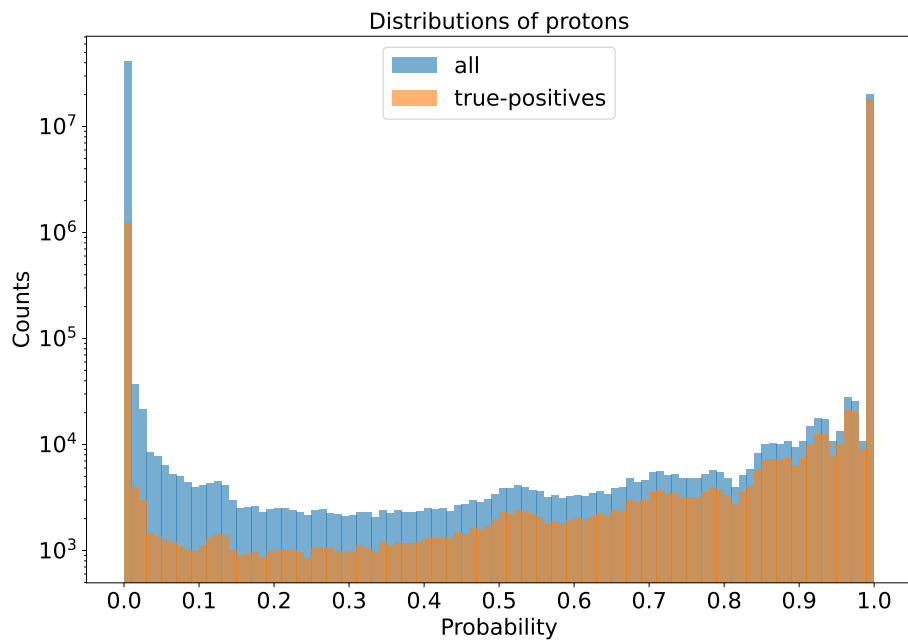


Figure 7.8: Probability distribution for ID=0

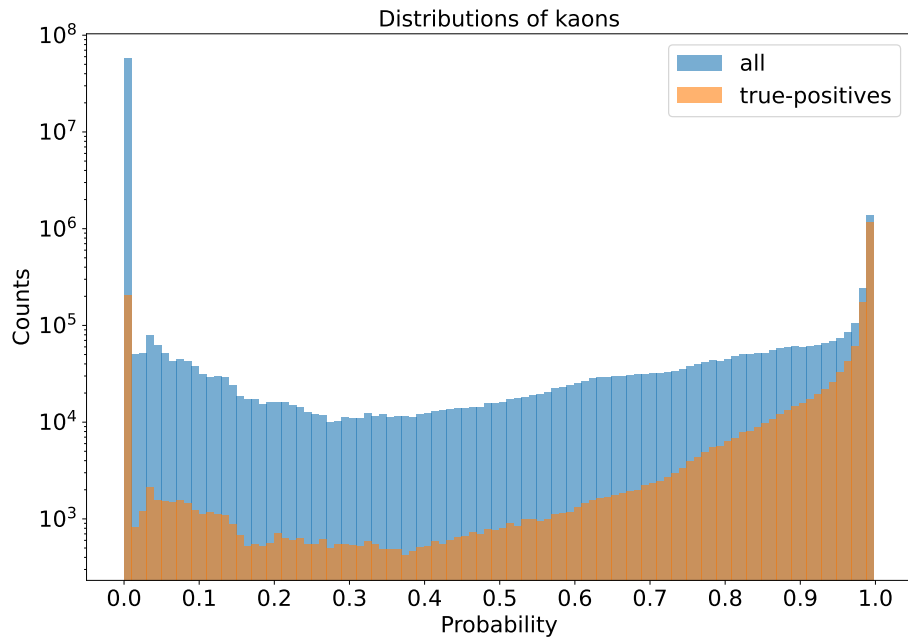


Figure 7.9: Probability distribution for ID=1

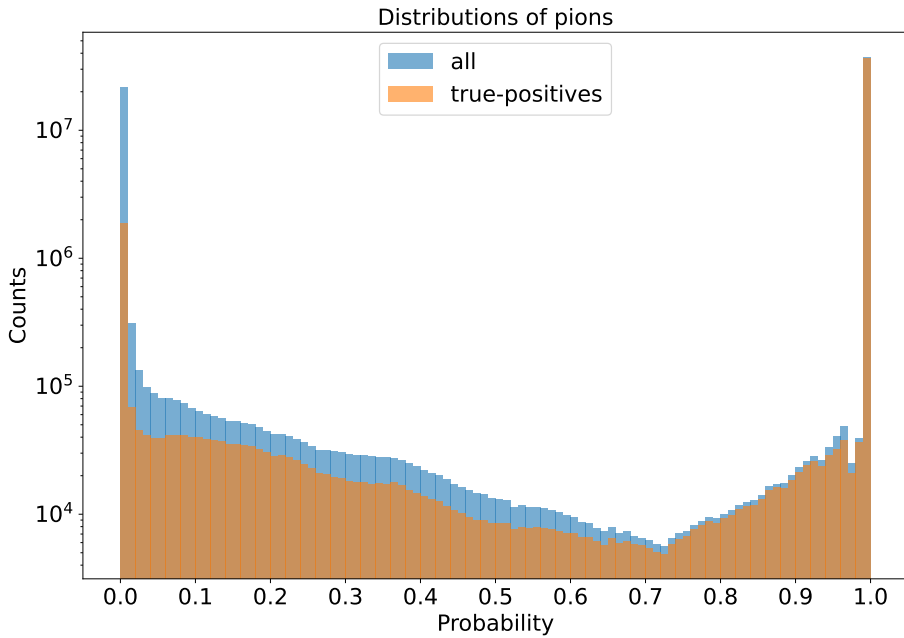


Figure 7.10: Probability distribution for ID=2

The following thresholds (which aim for as big efficiency as possible, with correct shape of mass-squared distribution (plotted later)): were decided:

- for ID = 0 : 0.88
- for ID = 1 : 0.96
- for ID = 2 : 0.82

### 7.2.2 Confusion matrix

The confusion matrix is useful in checking the accuracy of a classifier. By definition a confusion matrix  $C$  is such that  $C_{i,j}$  is equal to the number of observations known to be in group  $i$  and predicted to be in group  $j$ . Thus in binary classification, the count of true negatives is  $C_{0,0}$ , false negatives is  $C_{1,0}$ , true positives is  $C_{1,1}$  and false positives is  $C_{0,1}$ <sup>[34]</sup>. The normalised confusion matrix shows not the number of observations for each class, but the percentage.

For our model, the confusion matrices after applying the probability threshold are plotted on Figures 7.11 and 7.12.

Using the information from the confusion matrix, the efficiency of the classifier can be put in the Table 7.1.

Table 7.1: Efficiency of the ML model for TOF identification

ID	Efficiency	Efficiency of true positives	False/True ratio
0	108%	92.88%	0.17
1	119%	72.48%	0.65
2	102%	91.60	0.12

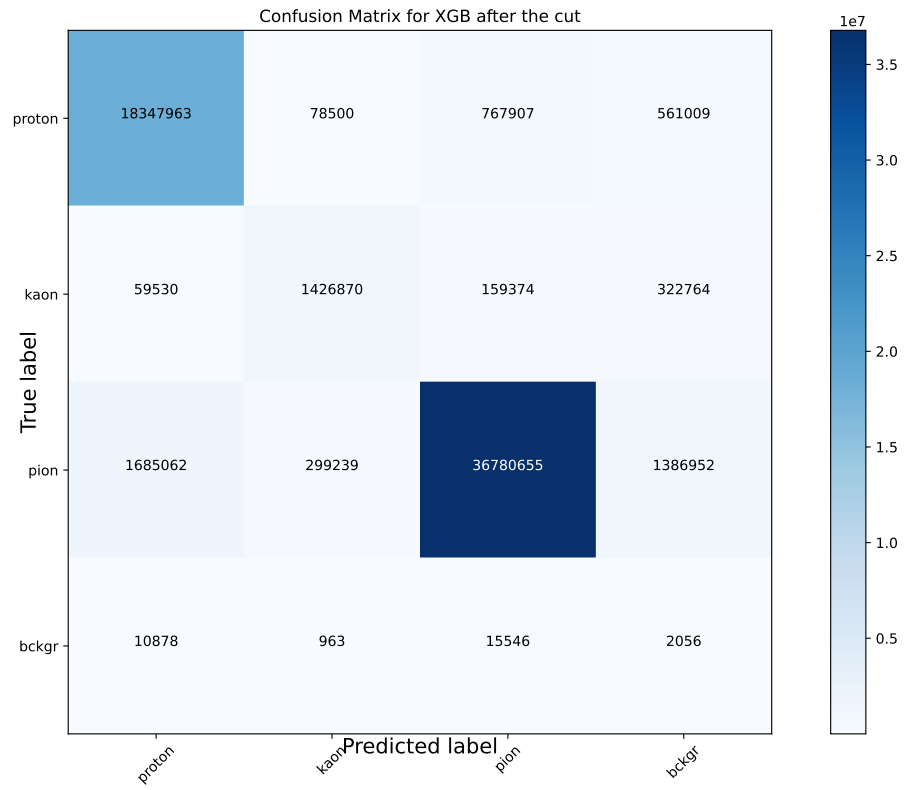


Figure 7.11: Confusion matrix

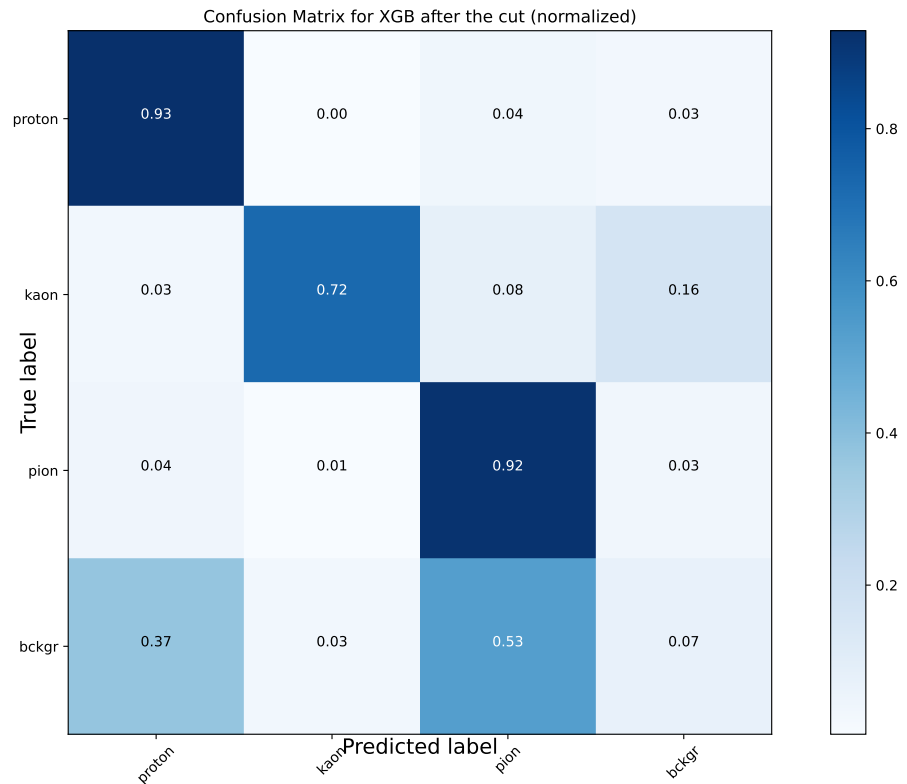


Figure 7.12: Confusion matrix (normalised)

### 7.2.3 Mass-squared distributions

After the ML model training and running it on the test dataset, the following invariant mass distributions are returned by it:

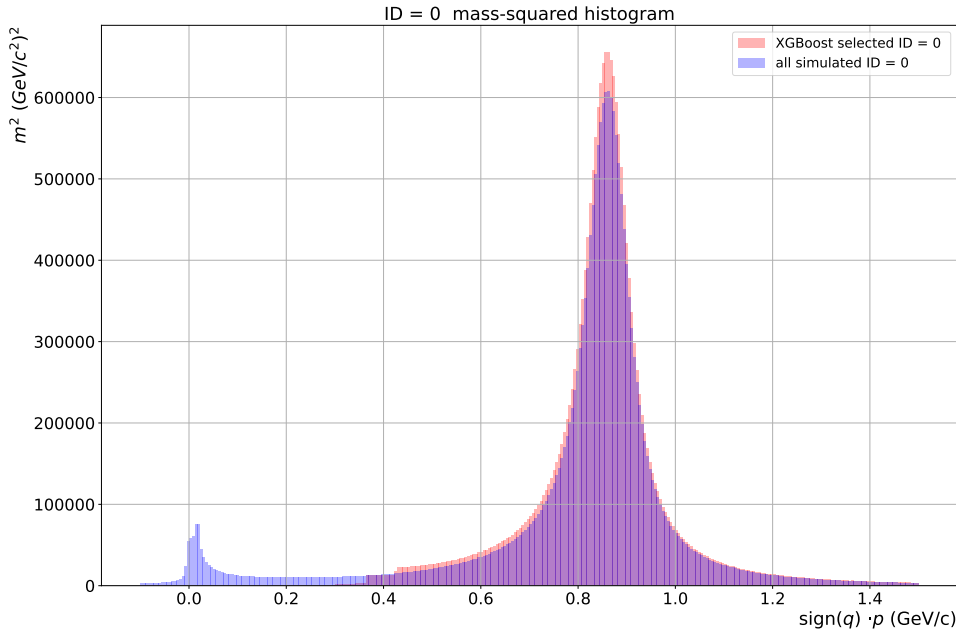


Figure 7.13: Mass-squared distributions for particles ID = 0

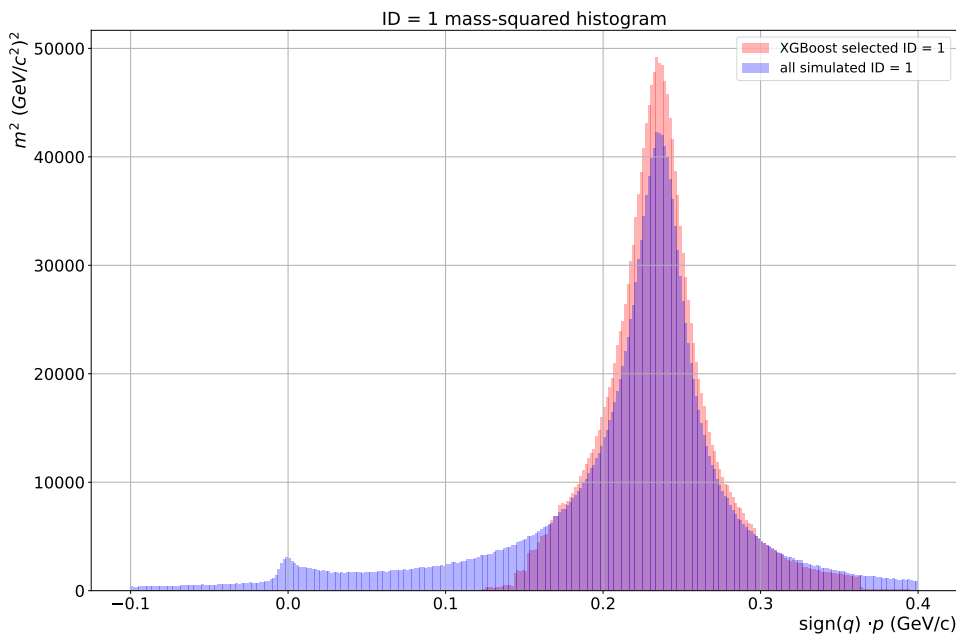


Figure 7.14: Mass-squared distributions for particles ID = 1

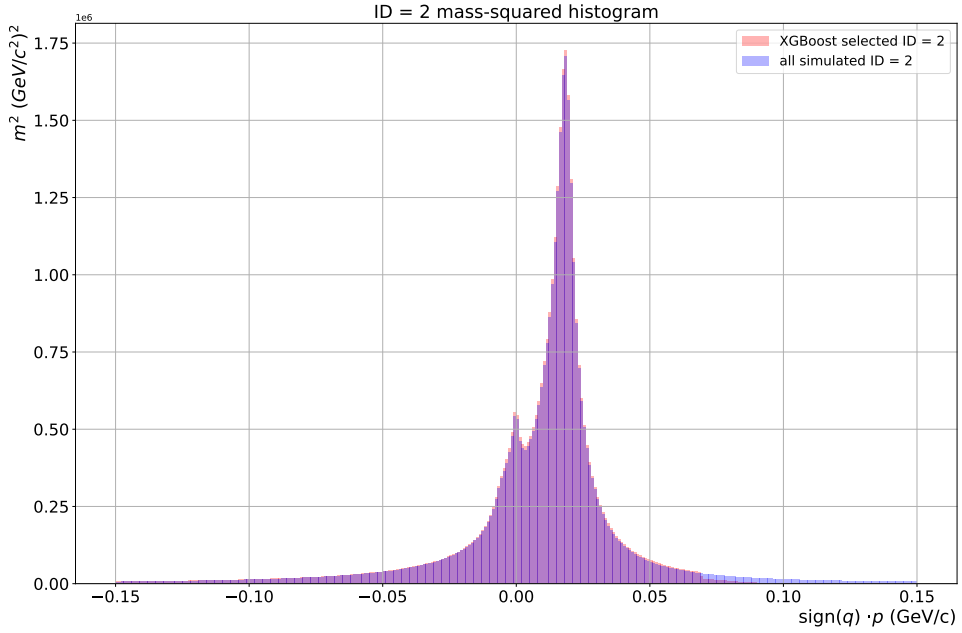


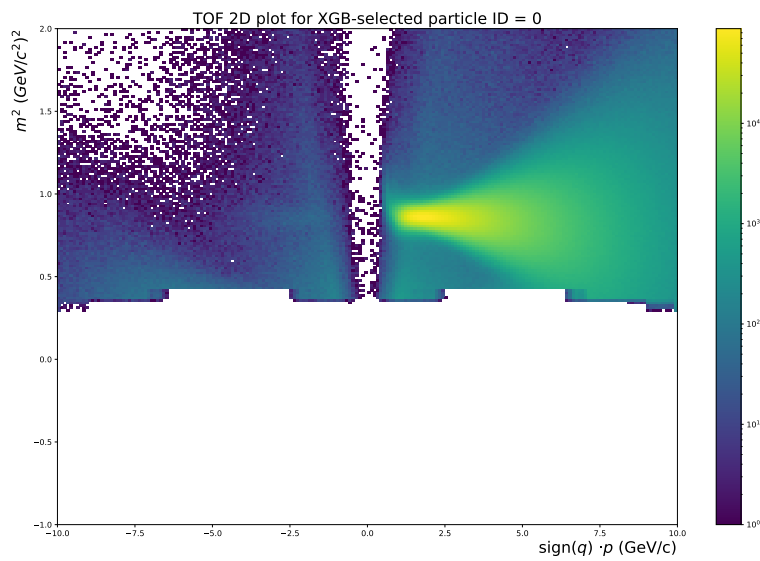
Figure 7.15: Mass-squared distributions for particles ID = 2

### 7.3 Analysis of the results

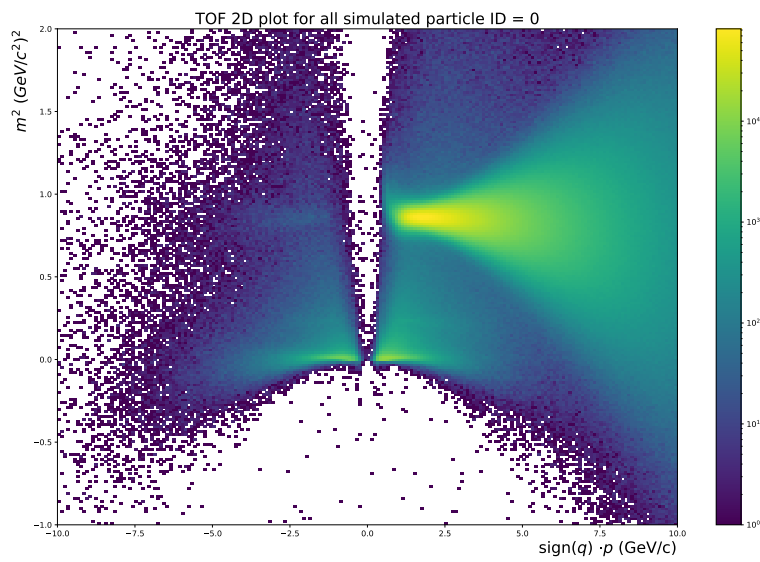
While the mass-squared distributions are useful, simple visualisation of the classifier results, the TOF plots are handier in analyzing the way the ML model works. The XGBoost-selected particles can be plotted with the simulated particles (all the particles that should be reconstructed) for each class.

#### ID = 0 (protons)

For particles ID = 0 (protons) we observe, that the protons of mass-squared close to 0 (mostly protons coming directly from the bullet particle) are not identified correctly. However, they should be treated as a different class, as the sigma-selection cuts them out during the training. For the same reason protons with high  $p$ , but small mass-squared are not identified at all.



(a) XGBoost selected particles



(b) Simulated particles

Figure 7.16: 2D TOF plot for ID = 0

## ID = 1 (kaons)

For particles ID = 1 (kaons) the efficiency, and the false-positive ratio are the most deviated from the correctness. The ML model with the high value of the threshold chosen picks only kaons with small  $p$  value. Also, one region of kaons close to  $m^2 = 2$  is also not used in training - however, it may be a result of a mismatch in the simulation, as the kaons are not expected in this region.

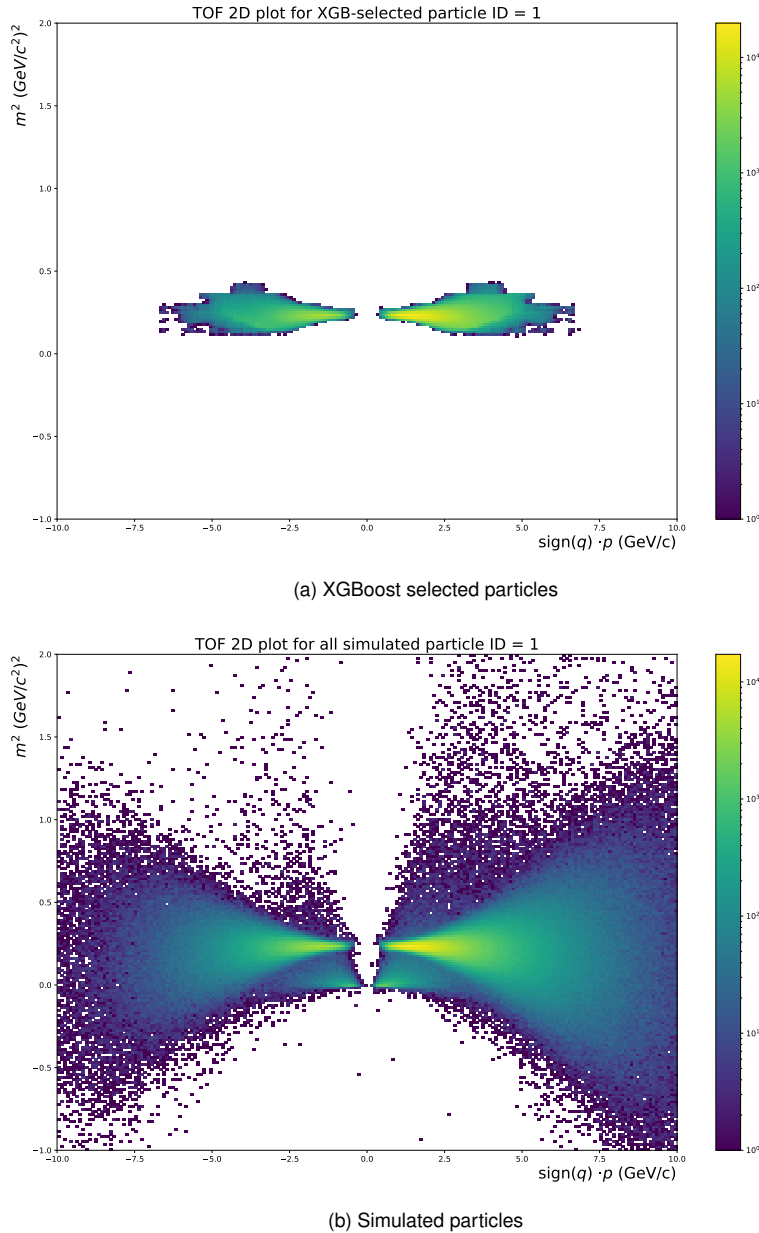


Figure 7.17: 2D TOF plot for ID = 1

## ID = 2 (pions, muons, and electrons)

For particles ID = 2 (pions, muons, and electrons) have the best efficiency, as most of the particles of the lower mass-squared values belong to one of these classes. Once again there is a region that is not expected - electrons of  $m^2 \approx 2$ , which are most probably a result of the mismatch in the simulation of the CBM setup.

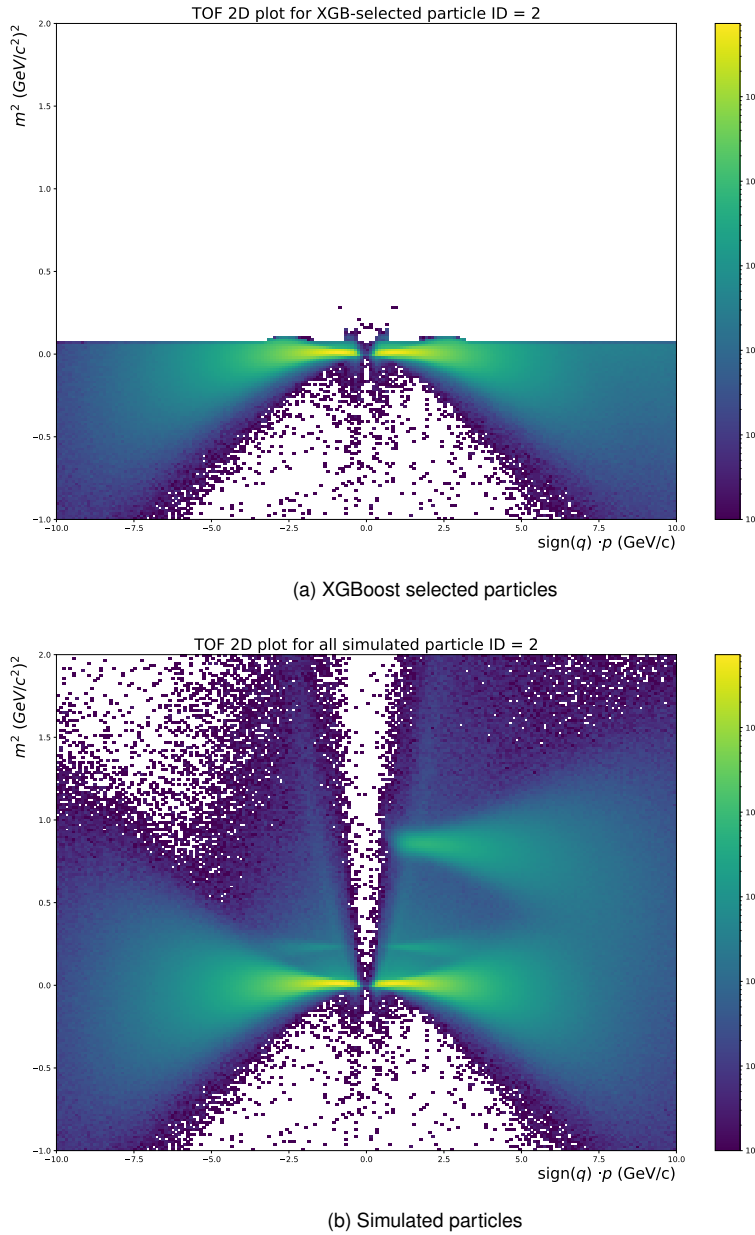


Figure 7.18: 2D TOF plot for ID = 2

### ID = 3 (background)

Particles ID = 3 (background) was mostly assigned to the particles of mass-squared close to the value of the mean mass-squared of kaons, but with bigger  $p$  values. It can also be seen in the confusion matrix - 0.14% of kaons are misidentified as background, as well as kaons and ID = 2 particles which, were found in this  $m^2$  region.

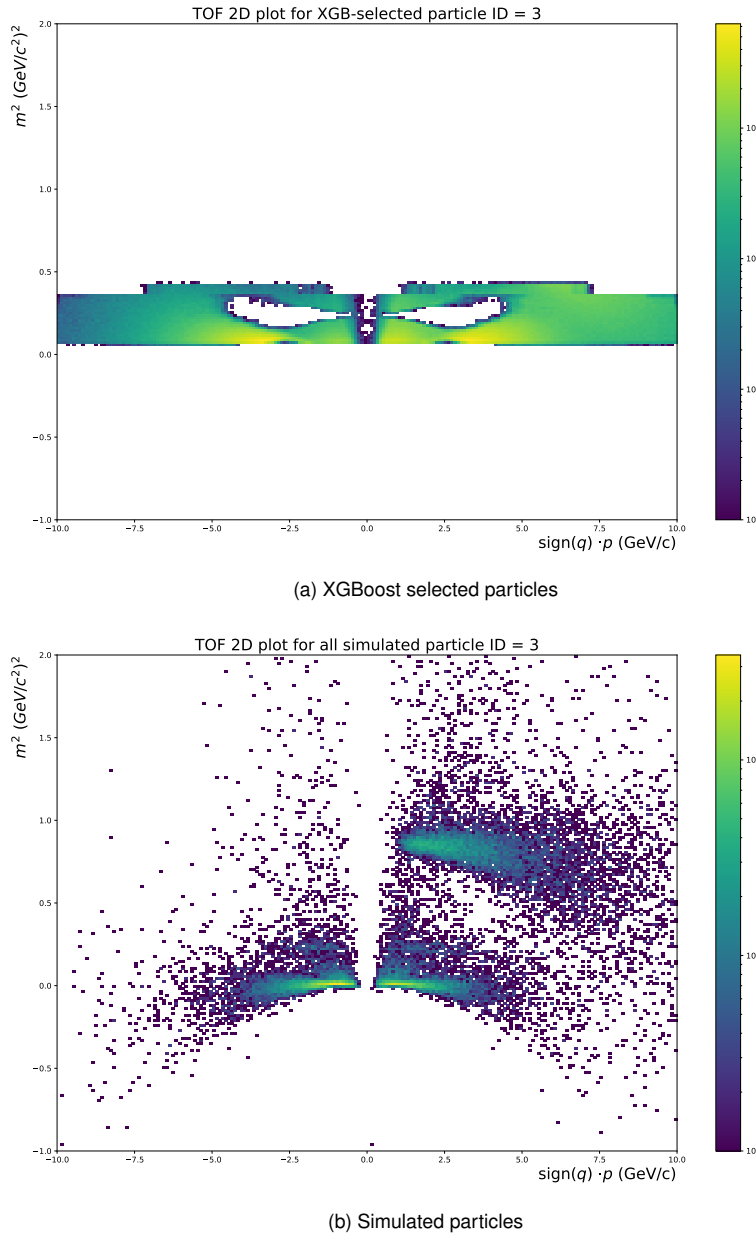


Figure 7.19: 2D TOF plot for ID = 3



# **Discussion and summary**

mogło być źle, ale będzie lepiej



# **Appendix A**

Kod rekonstrukcja kaonow ML



# **Appendix B**

Kod AnalysisTree->PlainTree



# **Appendix C**

Kod identyfikacja TOF ML



# Bibliography

- [1] Hanna Paulina Zbroszczyk. "Eksperimentalne aspekty badania korelacji femtoskopowych w zderzeniach relatywistycznych ciężkich jonów". Oficyna Wydawnicza Politechniki Warszawskiej, 2019, pp. 12, 24, 29.
- [2] D. Castelvecchi, "What's next for physics' standard model? Muon results throw theories into confusion," *Nature* **593** (2021) no.7857, 18-19 doi:10.1038/d41586-021-01033-8
- [3] wikipedia.org
- [4] Grebieszkow K.: "Fizyka zderzeń ciężkich jonów", Lectures at Faculty of Physics of WUT, <http://www.if.pw.edu.pl/kperl/HIP/hip.html>
- [5] "Compressed Baryonic Matter Experiment at FAIR, Progress Report 2020" Senger, Peter et. al (CBM Collaboration) doi:10.15120/GSI-2021-00421.
- [6] Angela Bracco (2017) "The NuPECC Long Range Plan 2017: Perspectives in Nuclear Physics", *Nuclear Physics News*, 27:3, 3-4, DOI: 10.1080/10619127.2017.1352311
- [7] CBM Collaboration, EPJA 53 3 (2017) 60 T.Galatyuk, NPA982 (2019), update (2021)
- [8] K. Aamodt *et al.* [ALICE], "The ALICE experiment at the CERN LHC," *JINST* **3** (2008), S08002 doi:10.1088/1748-0221/3/08/S08002
- [9] T. Ablyazimov *et al.* [CBM], "Challenges in QCD matter physics –The scientific programme of the Compressed Baryonic Matter experiment at FAIR," *Eur. Phys. J. A* **53** (2017) no.3, 60 doi:10.1140/epja/i2017-12248-y [arXiv:1607.01487 [nucl-ex]].
- [10] M. Orsaria, H. Rodrigues, F. Weber and G. A. Contrera, "Quark deconfinement in high-mass neutron stars," *Phys. Rev. C* **89** (2014) no.1, 015806 doi:10.1103/PhysRevC.89.015806 [arXiv:1308.1657 [nucl-th]].
- [11] fair-center.eu, accessed 9.12.2021
- [12] fair-center.eu/for-users/experiments/cbm.html, accessed 9.12.2021
- [13] S. A. Bass, M. Belkacem, M. Bleicher, M. Brandstetter, L. Bravina, C. Ernst, L. Gerland, M. Hofmann, S. Hofmann and J. Konopka, *et al.* "Microscopic models for ultrarelativistic heavy ion collisions," *Prog. Part. Nucl. Phys.* **41** (1998), 255-369 doi:10.1016/S0146-6410(98)00058-1 [arXiv:nucl-th/9803035 [nucl-th]]. ].

- [14] M. Baznat, A. Botvina, G. Musulmanbekov, V. Toneev and V. Zhezher, "Monte-Carlo Generator of Heavy Ion Collisions DCM-SMM," Phys. Part. Nucl. Lett. **17** (2020) no.3, 303-324 doi:10.1134/S1547477120030024 [arXiv:1912.09277 [nucl-th]].
- [15] Słodkowski M.: "Modelowanie Procesów Jądrowych", Lectures at Faculty of Physics of WUT, <http://efizyka.if.pw.edu.pl/MPJ>
- [16] S. Agostinelli *et al.* [GEANT4], "GEANT4—a simulation toolkit," Nucl. Instrum. Meth. A **506** (2003), 250-303 doi:10.1016/S0168-9002(03)01368-8
- [17] D. Blau, O. Golosov, E. Kashirin, V. Klochkov and I. Selyuzhenkov, "Performance studies for collective flow measurements with CBM at FAIR," J. Phys. Conf. Ser. **1390** (2019) no.1, 012027 doi:10.1088/1742-6596/1390/1/012027
- [18] <https://www.ibm.com/cloud/learn/machine-learning>, accessed 17.12.2021
- [19] A. L. Samuel, "Some Studies in Machine Learning Using the Game of Checkers," in IBM Journal of Research and Development, vol. 3, no. 3, pp. 210-229, July 1959, doi: 10.1147/rd.33.0210.
- [20] V. Chekalina, E. Orlova, F. Ratnikov, D. Ulyanov, A. Ustyuzhanin and E. Zakharov, "Generative Models for Fast Calorimeter Simulation: the LHCb case," EPJ Web Conf. **214** (2019), 02034 doi:10.1051/epjconf/201921402034
- [21] E. Lavrik, et. al., "Optical Inspection of the Silicon Micro-strip Sensors for the CBM Experiment employing Artificial Intelligence" arXiv:2107.07714
- [22] Chen, Tianqi, and Carlos Guestrin. "Xgboost: A scalable tree boosting system." Proceedings of the 22nd ACM SIGKDD international conference on knowledge discovery and data mining. 2016. [arXiv:1603.02754]
- [23] S. Khan, V. Klochkov, O. Lavoryk, O. Lubynets, A. I. Khan, A. Dubla and I. Selyuzhenkov, "Machine Learning Application for  $\Lambda$  Hyperon Reconstruction in CBM at FAIR," [arXiv:2109.02435 [physics.ins-det]].
- [24] <https://towardsdatascience.com/https-medium-com-vishalmorde-xgboost-algorithm-long-short-may-rein-edd9f99be63d>, accessed 18.12.2021
- [25] <https://xgboost.readthedocs.io/en/latest/parameter.html>, accessed 18.12.2021
- [26] [http://neupy.com/2016/12/17/hyperparameter\\_optimization\\_for\\_neural\\_networks.html](http://neupy.com/2016/12/17/hyperparameter_optimization_for_neural_networks.html), accessed 18.12.2021
- [27] Ostrowski J., "Particle Identification Framework extension for multidimensional fitting and mismatch studies", presentation on the 38th CBM Collaboration Meeting
- [28] <http://hyperphysics.phy-astr.gsu.edu/hbase/Particles/kaon.html>, accessed 19.12.2021

- [29] Zyzak, PhD thesis, 165 (2016)
- [30] Internal CBM documents: communication with O. Lubynets
- [31] Nowak J. "Optimizing K0S reconstruction at different collision energies using Machine Learning algorithms", Internship and Training Project Report from the Get\_Involved programme
- [32] [https://github.com/shahidzk1/CBM\\_ML\\_Lambda\\_Library.git](https://github.com/shahidzk1/CBM_ML_Lambda_Library.git)
- [33] <https://pdg.lbl.gov/2019/reviews/rpp2019-rev-monte-carlo-numbering.pdf>, accessed 27.12.2021
- [34] [https://scikit-learn.org/stable/modules/generated/sklearn.metrics.confusion\\_matrix.html](https://scikit-learn.org/stable/modules/generated/sklearn.metrics.confusion_matrix.html), accessed 27.12.2021



# List of Figures

2.1	Standard Model of Elementary Particles [3] . . . . .	15
2.2	Dependence of the color charge potential and the distance between the quarks and gluons. At long distances, the binding energy is too high and a new particle-antiparticle pair is created [4] . . . . .	17
2.3	Phase diagram of the QCD matter . . . . .	17
2.4	The "map" of the heavy-ion collision experiments [7] . . . . .	18
2.5	Particle population vs density (mixed-phase highlighted in yellow) [10] . . . . .	19
3.1	Map of FAIR[11] . . . . .	21
3.2	CBM setup[5] . . . . .	22
3.3	Visualisation of heavy-ion collisions in the URQMD model[15] . . . . .	23
4.1	Various surface defects on the silicon sensor identified using deep neural network[21] . . . . .	25
4.2	Evolution of XGBoost Algorithm from Decision Trees[24] . . . . .	26
5.1	2D TOF plot with pions, kaons, and protons shown . . . . .	30
5.2	$K_S^0$ main decay mode [28] . . . . .	30
5.3	Decay scheme and topological variables of a $K_S^0$ decay in the PFSimple . . . . .	31
5.4	Example of a decision tree using manual selection criteria . . . . .	32
5.5	Example of distributions to be checked with the manual selection criteria optimization . . . . .	32
6.1	Data enriching . . . . .	34
6.2	Correlation matrix . . . . .	37
6.3	Correlation of all variables with mass . . . . .	38
6.4	Receiver Operating Characteristic . . . . .	39
6.5	Probability plot . . . . .	39
6.6	Invariant mass distribution . . . . .	40
6.7	Comparison with KFPF cuts . . . . .	41
6.8	Invariant mass distribution for probability > 0.86 . . . . .	42
6.9	True-false positives investigation . . . . .	43
6.10	Comparison with KFPF cuts for 3.3A GeV/c . . . . .	45
6.11	Invariant mass distribution for different MF scaling . . . . .	46

7.1	Histograms of mass-squared of each particle class (differences of quantity of each particle type can also be observed) . . . . .	47
7.2	2D TOF histogram of all particles after data cleaning . . . . .	49
7.3	2D TOF histogram of protons (ID=0) after $1\sigma$ selection . . . . .	49
7.4	2D TOF histogram of kaons (ID=1) after $1.5\sigma$ selection . . . . .	50
7.5	2D TOF histogram of pions, muons and electrons (ID=2) after $1\sigma$ selection . . . . .	50
7.6	Correlation matrix . . . . .	51
7.7	Probabilities distribution for all the classes . . . . .	52
7.8	Probability distribution for ID=0 . . . . .	53
7.9	Probability distribution for ID=1 . . . . .	53
7.10	Probability distribution for ID=2 . . . . .	54
7.11	Confusion matrix . . . . .	55
7.12	Confusion matrix (normalised) . . . . .	55
7.13	Mass-squared distributions for particles ID = 0 . . . . .	56
7.14	Mass-squared distributions for particles ID = 1 . . . . .	56
7.15	Mass-squared distributions for particles ID = 2 . . . . .	57
7.16	2D TOF plot for ID = 0 . . . . .	58
7.17	2D TOF plot for ID = 1 . . . . .	59
7.18	2D TOF plot for ID = 2 . . . . .	60
7.19	2D TOF plot for ID = 3 . . . . .	61

# List of Tables

4.1 Comparison of hyperparameters optimization methods . . . . .	27
6.1 Advantages and disadvantages of ML selection criteria optimization . . . . .	33
6.2 Comparison of MF strength vs. efficiency . . . . .	44
7.1 Efficiency of the ML model for TOF identification . . . . .	54